iScience

CellPress
OPEN ACCESS

Article

Stability of high-entropy alloys under electrocatalytic conditions

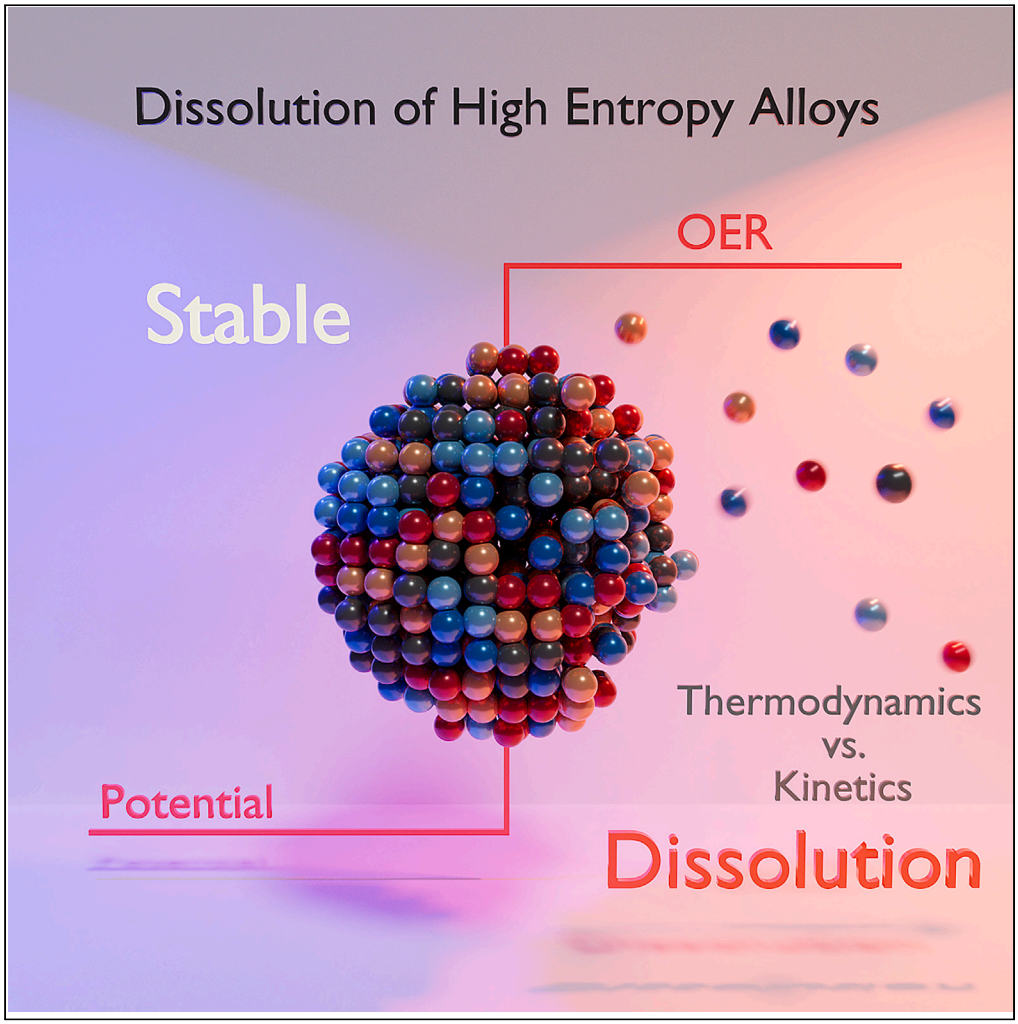

Attila Kormányos, Qi Dong, Bin Xiao, ..., Liangbing Hu, Alfred Ludwig, Serhiy Cherevko

kormanyos.attila@szte.hu (A.K.)
s.cherevko@fz-juelich.de (S.C.)

Highlights

Synthesis of single-phase multimetallic thin films and carbon-supported nanoparticles

Stability screening using on-line inductively coupled plasma mass spectrometry

Stability screening under conditions typically employed in electrocatalytic experiments

Thermodynamic contributions were outperformed by kinetic effects

Kormányos et al., iScience *26*, 107775
October 20, 2023 © 2023 The Author(s).
https://doi.org/10.1016/j.isci.2023.107775

iScience

CellPress
OPEN ACCESS

Article

Stability of high-entropy alloys under electrocatalytic conditions

Attila Kormányos,[1,2,7,*] Qi Dong,[3] Bin Xiao,[4] Tangyuan Li,[3] Alan Savan,[4] Ken Jenewein,[1,5] Tatiana Priamushko,[1] Andreas Körner,[1] Thomas Böhm,[1] Andreas Hutzler,[1] Liangbing Hu,[3,6] Alfred Ludwig,[4] and Serhiy Cherevko[1,*]

SUMMARY

High-entropy alloys are claimed to possess superior stability due to thermodynamic contributions. However, this statement mostly lies on a hypothetical basis. In this study, we use on-line inductively coupled plasma mass spectrometer to investigate the dissolution of five representative electrocatalysts in acidic and alkaline media and a wide potential window targeting the most important applications. To address both model and applied systems, we synthesized thin films and carbon-supported nanoparticles ranging from an elemental (Pt) sample to binary (PtRu), ternary (PtRuIr), quaternary (PtRuIrRh), and quinary (PtRuIrRhPd) alloy samples. For certain metals in the high-entropy alloy under alkaline conditions, lower dissolution was observed. Still, the improvement was not striking and can be rather explained by the lowered concentration of elements in the multinary alloys instead of the synergistic effects of thermodynamics. We postulate that this is because of dissolution kinetic effects, which are always present under electrocatalytic conditions, overcompensating thermodynamic contributions.

INTRODUCTION

(Photo)Electrocatalysis is one of the most attractive ways to convert the energy of sunlight for storage in the form of chemical bonds.[1] In this vein, hydrogen, and oxygen evolution reactions (i.e., water splitting; HERs and OERs, respectively) and CO_2 reduction (CO2RR) are promising directions. However, all of these are thermodynamically uphill and kinetically sluggish processes; therefore, to drive them efficiently, there are a considerable number of requirements that a good electrocatalyst candidate has to simultaneously fulfill. To cut this Gordian knot, in the past couple of decades, a significant amount of research effort has been dedicated to finding electrocatalysts that actively and selectively catalyze the aforementioned processes. Up to date, none of the single elements and simple alloys (up to three main elements, occasionally with some further dopants added) have proven to be ideal candidates for these reactions. Therefore, attention in the field lately shifted toward synthesizing systems with higher complexity. This could mean, for example, increasing the electrochemically active surface area (ECSA), hence the number of active sites by nanostructuring[2] to tailor the surface composition of the synthesized alloy by various physicochemical processes adjusting selectivity or protecting the electrocatalyst surface.[3,4] In addition to this, a rather novel trend is to increase the number of alloy constituents further, developing multinary systems composed of more than three distinct elements, most frequently in *comparable amounts*.[5] High-entropy alloys (HEAs)[6] or compositionally complex solid solutions belong to this category where the number of constituents is five or more and all elements are homogeneously mixed in a single phase (the highest number of elements in a single HEA phase so far is 15[7]), most frequently fcc or bcc. Although HEAs were first synthesized less than 20 years ago,[7,8] research interest has shown a great increase in the past five years.[9–11] This is not surprising considering the numerous synergistic features that can emerge upon the formation of a HEA phase.[5,12] By systematically designing the HEA composition, binding energies (the result of short- and long-range interactions between the atoms and their neighbors) can be tailored to the desired application and help break scaling relations.[13,14] Additionally, multiple reactions could be simultaneously catalyzed due to the heterogeneity of active sites opening the possibility to drive cascade reactions such as CO_2 reduction or the electrooxidation of alcohols.[15,16] Finally, from a *purely thermodynamic standpoint*, HEAs are materials that could show remarkably high stability. Since mixing enthalpy is generally considered negligible for single-phase complex solid solutions,[10] this increase in stability is probably due to stabilization by high configurational entropy (above 1.5R, where R is the gas constant[12]) preventing fatal degradation processes such as the Kirkendall effect or dealloying.[17] The validity of this statement started to be addressed experimentally in recent research projects under conditions typically occurring in electrocatalytic

[1]Forschungszentrum Jülich GmbH, Helmholtz Institute Erlangen-Nürnberg for Renewable Energy (IEK-11), Cauerstraße 1, 91058 Erlangen, Germany
[2]Department of Physical Chemistry and Materials Science, University of Szeged, Aradi sq. 1, 6720 Szeged, Hungary
[3]Department of Materials Science and Engineering, University of Maryland, College Park, MD 20742, United States
[4]Materials Discovery and Interfaces, Institute for Materials, Ruhr-Universität Bochum, 44801 Bochum, Germany
[5]Department of Chemical and Biological Engineering, Friedrich-Alexander-Universität Erlangen-Nürnberg, Egerlandstr. 3, 91058 Erlangen, Germany
[6]Center for Materials Innovation, University of Maryland, College Park, MD 20742, United States
[7]Lead contact
*Correspondence: kormanyos.attila@szte.hu (A.K.), s.cherevko@fz-juelich.de (S.C.)
https://doi.org/10.1016/j.isci.2023.107775

This is an open access article under the CC BY-NC-ND license (http://creativecommons.org/licenses/by-nc-nd/4.0/).

processes.[18–21] However, it has to be noted that these efforts were not the main topic of these papers; their goal was to showcase electrochemical stability without diving deeper to understand the underlying phenomena.

Electrocatalyst stability in technological systems (e.g., electrolyzers, fuel cells, etc.) is notably influenced by several parameters such as electrolyte composition and pH, temperature, pressure, applied current density or potential, etc.[22] Furthermore, these devices operate far from equilibrium (e.g., large cell voltage and high current densities) meaning that kinetics is at least as important a factor as thermodynamics in assessing electrocatalyst stability. While thermodynamic stability descriptors for single metals and metal alloys can be estimated with relative ease,[23–25] kinetic contributions are almost impossible to predict in such systems, especially due to the lack of an adequate amount of experimental data. However, modeling the electrocatalytic activity and stability of HEAs is in its infancy[24] due to their complex and diverse surface properties. There is a moderate amount of experimental data available assessing the stability of single transition metal catalysts under conditions (potential window, electrolyte, pH, etc.) occurring in electrocatalytic processes.[26,27] Moreover, a clear correlation was described recently between the cohesive energy of metals (3–5d transition metals), their oxygen adsorption energy, and the amount of metal dissolved transiently under the performed electrochemical protocols.[28] It was shown that intrinsic metal properties like the M-M and M-O bond strength can be effectively used as stability descriptors for d-metals.[29] Stability of single-phase, binary alloys is much less investigated. One of the main issues is that stability data are collected only for a few distinct compositions instead of covering the entire composition range. Still, there are already a few examples utilizing high-throughput (HT) screening[30,31] to determine the activity and stability of binary alloys in a wide composition range. Data on stability are only scarcely reported when the number of alloy constituents exceeds three. Some data exist for systems where the alloy consists of two main elements (such as Pt and Ni in the case of oxygen reduction electrocatalysts) and the third (in some rare cases fourth) element is present as a dopant (only a few atomic percent) in the alloy to boost either the activity or stability of the system.[32,33] Complexity exponentially increases with the number of elements in the alloy; thus, it is not surprising that no example in the literature has been presented so far investigating the stability of HEAs under electrocatalytic conditions. The superior electrocatalytic activity of HEAs was already demonstrated, for example, in electrocatalytic methanol[34–36] and ethanol[15,16] oxidation, in the oxygen reduction reaction (ORR)[37] and in the CO2RR,[38] etc. In addition to this, factors governing the stability of HEAs inevitably have to be studied and understood to fully realize their potential and future industrial application.

The traditional way of benchmarking the stability of electrocatalysts is typically done by performing accelerated stress test (AST) protocols and measuring the activity (e.g., by collecting a linear sweep voltammogram or cyclic voltammogram in the potential window of interest or checking the overpotential at a fixed current density) before and after. AST protocols could involve either fast potential cycling or chronoamperometric/chronopotentiometric measurements for several hours.[33,39–42] Electrochemical measurements are usually followed by the characterization of the catalyst films by several *ex situ* techniques such as scanning and transmission electron microscopy (SEM and TEM, respectively) combined with energy-dispersive X-ray (EDX) photoelectron spectroscopy, X-ray photoelectron spectroscopy (XPS), Raman spectroscopy, or other measurement methods.[41,42] However, all of them are *ex situ* methods necessitating the removal of the catalyst layer from the cell or tedious sample preparation (e.g., drop-casting onto a TEM grid, etc.) prior to the measurements. Even exposing the samples to air could induce a change in the surface composition of the samples by forming, for example, oxides at their surface. Thus, all the aforementioned practices give only indirect information on the degradation mechanism of the given electrocatalyst.

To uncover the dissolution/degradation mechanism of HEAs under process conditions, *in situ* techniques must be employed. One of these is a scanning flow cell (SFC) coupled to an inductively coupled plasma mass spectrometer (on-line ICP-MS). This technique allows us to simultaneously run electrochemical measurements and to detect even trace amounts of metals (down to pg cm^{-2}) dissolved during a protocol. As HEAs consist of at least five different elements, conclusions regarding the factors affecting their stability can only be made if the widest possible composition range is studied. It is impossible to characterize such an amount of electrocatalysts in a "trial and error" manner; experimental and data analysis protocols at least partially have to be automated. Our on-line ICP-MS setup is equipped with a small area flow cell along with a 3D translational stage which allows performing activity and stability measurements for an entire materials library in a high-throughput manner.[43,44] More information on on-line ICP-MS and its various applications can be found in our earlier studies.[27,28,45]

In this contribution, we assessed the stability of five electrocatalysts employing on-line ICP-MS, starting from an elemental sample (Pt) and then adding additional elements (Ru, Ir, Rh, and Pd) to yield binary (PtRu), ternary (PtRuIr), and quaternary (PtRuIrRh) samples as well as a quinary HEA sample (PtRuIrRhPd). All samples contain each metal in equal molar fractions because according to the literature these compositions would lead to the most stable electrocatalysts thanks to thermodynamic contributions.[10,12] Two types of samples were studied:

i) thin films prepared by magnetron co-sputtering[46] and
ii) carbon-supported nanoparticles (NPs) synthesized by carbothermal shock synthesis.[9,11] Magnetron co-sputtering allows the one-step synthesis of metal alloy samples. The resulting samples are uniform, and the synthesis method is highly reproducible. The method allows the synthesis of material libraries on a single wafer that can be further characterized/tested by physical or (electro)chemical methods in a high-throughput manner, making magnetron co-sputtering a viable tool to synthesize and explore HEAs in a wide composition range. An additional advantage is that there are no sample preparation steps necessary prior to electrochemical measurements (e.g., ink preparation, spray-coating/drop-casting, etc.). On the other hand, while sputtered samples are ideal model systems yielding information with fundamental value, one has to be careful transferring the gained knowledge to "real", frequently NP-based systems. In systems such as fuel cells or continuous-flow electrolyzers, either alloy NPs or their carbon-supported counterparts are used as electrocatalysts; thus, studying their stability is equally important. In this regard, we employed a high-temperature thermal shock approach to synthesize multielement NPs, which is known to offer good NP quality in terms of size, size distribution, and elemental uniformity.[47,11]

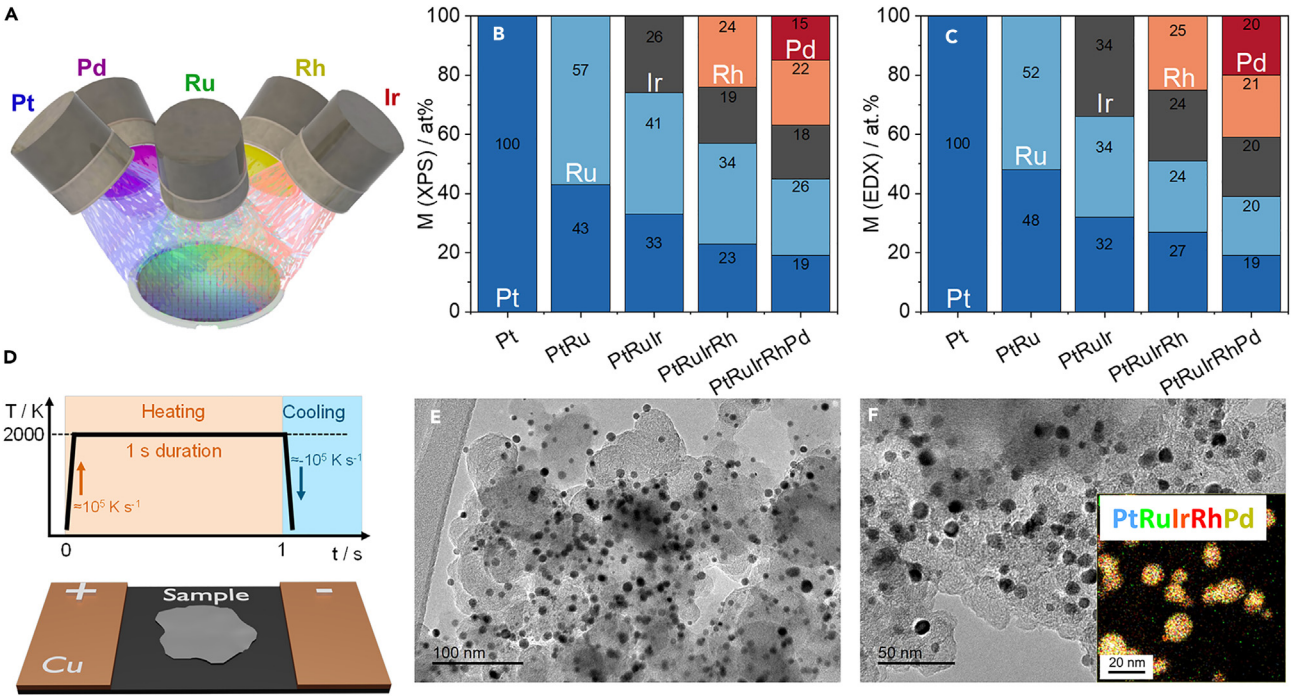

Figure 1. Physical and morphological analysis of the synthesized samples

(A–C) Schematic representation of the confocal magnetron sputtering configuration employing 5 cathodes. Surface (B) and bulk composition (C) of the sputtered thin film samples prepared by magnetron co-sputtering with rotating the substrate by 10 rpm.

(D–F) Schematic representation of the carbothermal shock synthesis setup and a typical temperature profile employed during the synthesis of the carbon-supported nanoparticles. TEM images captured from the carbon-supported Pt (E) and PtRuIrRhPd (F) samples. The inset shows an HAADF-STEM and EDX image gathered for the PtRuIrRhPd sample.

Both synthesis methods employed in our study are non-equilibrium, allowing the preparation of perfectly mixed, homogeneous complex alloy systems in a single phase (miscibility gaps in the phase diagrams can be overcome).

The main goal of this work was to determine whether HEAs show enhanced stability (predicted so far only theoretically) under electrocatalytic conditions compared to other multinary systems (up to ternary) containing the same elements in the same elemental ratio. In addition to this, by studying the stability of thin films and carbon-supported NPs, we investigated if findings based on thin film model systems could be transferred to the ones closer to possible future applications. To do so, on-line ICP-MS measurements were performed in both acidic and alkaline media and in a wide potential window covering that typically occurring in HER, ORR, and OER. Hence, the dissolution stability results from this work are considered of general interest for a broad electrochemical energy conversion and storage community.

RESULTS

Physical and morphological characterization

Five different thin films (Pt, binary PtRu, ternary PtRuIr, quaternary PtRuIrRh, and quinary PtRuIrRhPd) in equiatomic compositions in the case of the alloys were fabricated using a magnetron sputtering system (a schematic representation is presented in Figure 1A) by co-deposition from confocally placed elemental targets. In addition to the equiatomic conditions, two binary PtRu samples were fabricated with the compositions $Pt_{20}Ru_{80}$ and $Pt_{80}Ru_{20}$. High-purity targets (Rh: 99.99%, Ir: 99.9%, Pd: 99.99%, Pt: 99.99%, Ru: 99.95%) were used. Except for the Rh target which has a 2-inch diameter, all other elements were sputtered from 4-inch diameter targets. Each target was positioned with an inclination angle of around 45° with respect to the substrate. Prior to the deposition, the chamber vacuum was on the order of 10^{-5} Pa. During deposition, the pressure was set to 0.667 Pa (Ar, 99.9999%), and the substrate was rotated at the rate of 10 rpm to ensure compositional uniformity. The detailed sputter information such as power type and sputter powers are listed in Table S1. The power applied to each cathode was adjusted to yield approximately equiatomic compositions, and the deposition time was set so that the thin films were on the order of 100 nm thickness. Theoretical calculations suggest that the combination of Pt, Ru, Ir, Rh, and Pd should yield a perfectly mixed homogeneous, single-phase solid solution.[14] This was also experimentally validated for a similar system by atom probe tomography.[46] The surface and bulk composition of the sputtered samples were determined with XPS and EDX spectroscopy (Figures 1Band 1C). Based on these measurements, the surface composition of the prepared samples is slightly different from the bulk composition; the electrocatalyst surface appears to be slightly richer in Ru regardless of the number of constituents. Ru is the most oxophilic element within the 5 constituents; therefore, when the samples are stored

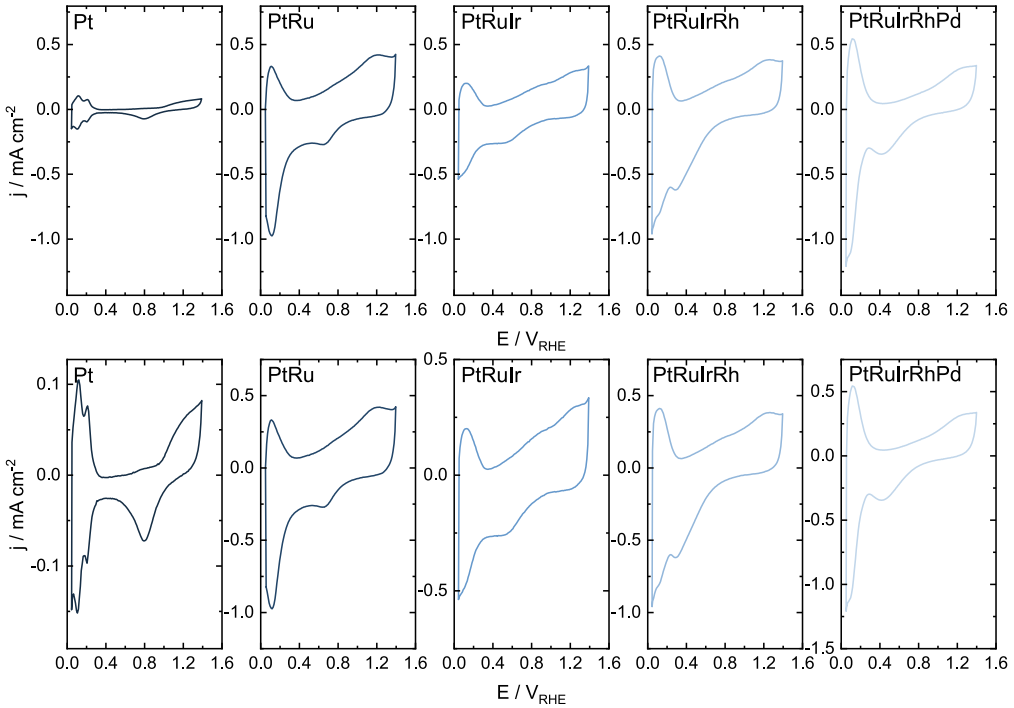

Figure 2. Cyclic voltammetry results recorded for all samples ranging from unary to quinary compositions

CVs recorded for the thin films (top row) and for the carbon-supported nanoparticles (bottom row) in 0.1 M $HClO_4$ electrolyte solution in between 0.05 V_{RHE} and 1.4 V_{RHE}, applying 200 mV s^{-1} scan rate. The electrolyte solution was saturated with Ar.

under ambient conditions (O_2 presence), Ru atoms could migrate to the surface of the catalyst.[48] Because the samples were stored under air after synthesis, their surface was inherently covered by a thin layer of native oxide layer. Since the surface plays the dominant role in electrocatalytic reactions, surface compositions measured by XPS were used in all further calculations and for all following figures containing data derived for the sputtered samples.

The carbon-supported NPs were prepared using carbothermal shock synthesis.[11] This employs a two-step flash (on the order of 10^4 K s^{-1}) heating and cooling protocol along with a hold at approximately 2,000 K for 1,000 ms (the schematic representation of sample preparation and the temperature profile are presented in Figure 1D) on a carbon support yielding multimetallic and, importantly, single-phase NPs. In our study, we reproduced the synthesis protocol described earlier.[11] The synthesis of multinary electrocatalyst samples (especially for the elements employed in our experiments) has been extensively studied since then. Thus, it can be firmly stated that the quality (composition and particle size distribution) of the resulting NPs is in good control by the standard synthesis parameters. This means that the nominal composition of the synthesized unary and multinary systems is close to identical to the real composition (evidenced by numerous in-depth material characterizations presented in precedent studies).[11,47,49] Composition and homogeneity of the synthesized multinary samples were mapped with STEM-EDX (results are presented in Figure S1). Measurements confirmed the homogeneous, uniform distribution of all metal constituents in the nanocrystals. Moreover, no phase segregation can be spotted, and all NPs appear as a single-phase solid solution. The metal loading of the carbon-supported NPs was fixed at 20 wt %; higher metal loadings resulted in the aggregation of the NPs and the subsequent alteration of their size distribution. The morphology of the prepared samples was mapped with TEM. TEM images captured from the Pt/C and PtRuIrRhPd/C samples are presented in Figures 1E and 1F. It is visible that the metal NPs are evenly distributed on the carbon support (Vulcan XC72). The NPs in both the unary and multinary samples bear with narrow size distribution following a bimodal trend: bigger NPs with an average diameter of 7–8 nm and several smaller NPs with around 1 nm diameter. One possible reason behind the formation of the smaller NPs is the carbon support. It might have contained various defect sites. Some of these facilitated the formation of smaller NPs, while others favored the formation of bigger NPs (by adsorbing more precursors around it). Since the carbon support was from a commercial source, we believe that such fluctuations in its quality might have happened. Still, even the smallest multimetallic NPs bear an equimolar composition (Figure S1).

General electrochemical behavior

The general electrochemical behavior of both the thin films and the carbon-supported NPs was investigated with cyclic voltammetry (CV). Measurements were performed in a sealed electrochemical cell in which the electrolyte was saturated with Ar. Results obtained for the thin films and the carbon-supported NPs in acidic media are presented in Figure 2 (for the data recorded in 0.05 M KOH see Figure S2). It

is visible in Figure 2, top row that the CV recorded for the Pt film shows typically observed features for Pt (hydrogen adsorption and desorption region, Pt oxidation and PtO_x reduction).[50,51] By increasing the number of alloy constituents, several changes can be observed: the peaks resembling the weak and strong adsorption of hydrogen merged and their area increased considerably. Moreover, the peak corresponding to oxide reduction shifted toward less positive potentials, which was already observed for binary Pt alloys such as PtIr.[31] The most striking difference is that the area of the CVs increased significantly by the addition of further elements. This is especially true for the hydrogen underpotential deposition (H_{UPD}) region, which indicates a notable increase in the ECSA by the number of alloy constituents. Similar conclusions can be made for the CVs recorded in alkaline media (Figure S2A). The higher ECSA can be explained by a change in surface roughness, which was evidenced by atomic force microscopy (AFM) measurements (Figure S3). According to these results, the mean roughness of all samples including the HEA remained below 1 nm indicating a smooth surface (Figure S4). The only outlier is Pt, which shows a mean roughness below 0.4 nm, while the mean roughness of all the other samples is centered around 0.5 nm. To further study this observation, H_{UPD} peaks were integrated both in acidic and alkaline media (Figures S4A and S4B). Since it is impossible to correctly determine the actual ECSA from the H_{UPD} area in the case of the multinary samples, all calculated values were normalized to those obtained for Pt. It is seen that the normalized H_{UPD} area closely follows the trend found by AFM measurements (Figure S4C).

Similar observations can be made in terms of the change in the H_{UPD} region along with the shift of the oxide reduction peak for the carbon-supported NPs. However, in contrast to the thin films, the area of all CVs is more or less similar. This finding is also reflected in the normalized H_{UPD} area data where the values calculated for the multinary NP samples are centered around 1. The reason behind this is that while crystallite sizes in the case of the sputtered films show big differences depending on the number of elements present, the size of the NPs synthesized by the carbothermal shock method remained similar regardless of the number of metal constituents resulting in a more constant ECSA. As mentioned earlier, the position (potential) of the peak corresponding to the reduction of the surface oxide layer has also shifted with the number of metals in the alloy. It is visible in Figure S5A that the potential of the peak shifted monotonically to less negative potentials from 0.8 V_{RHE} (Pt) to 0.3–0.4 V_{RHE} (PtRuIrRh) and increased slightly only for the HEA sample. pH had a notable effect on the oxide reduction peak potential in the case of the unary (around 100 mV smaller peak potential in 0.05 M KOH), quaternary, and HEA sample (around 100 mV higher peak potential in alkaline media for both samples). Identical trends can be observed for the carbon-supported samples (Figure S5B); however, the difference between the values obtained for the Pt and PtRuIrRh samples ($\Delta E \approx 300$ mV) is smaller. Finally, the deviation caused by the pH in the position of the oxide reduction peak is also smaller for the carbon-supported NPs compared to the thin films. All in all, the shift in the oxide reduction peak to less positive potentials indirectly suggests that alloying might have a beneficial effect on "global" stability. This is in line with the theoretical predictions published earlier. As a next step, the stability of the monometallic and alloy samples was monitored with on-line ICP-MS under electrocatalytic conditions.

Stability of the thin films

To map the stability of the pristine metals and the alloy samples, the outlet of the scanning flow cell (SFC) was coupled to the inlet of an ICP-MS. This combination allowed the real-time tracking of the dissolution of each metal. Sputtered thin films are considered excellent model systems. Thanks to the single-step synthesis, the resulting electrode is homogeneously coated with the single-phase metal alloy thin film in which the atoms are evenly distributed (see discussion earlier on the differences in the roughness) and all samples yield comparable electrodes facilitating systematic characterization. Based on this, our assumption was that emerging trends (if there are any) in stability by systematically increasing the number of alloy constituents could be observed. Thus, as a first step, the stability of the thin films was studied. Two electrochemical protocols covering a broad potential window were carried out to gain deeper insights on the alloys' stability in different applications. The first protocol consisted of three CVs starting at 0.05 V_{RHE}, applying a scan rate of 5 mV s^{-1} and going to three, gradually increasing upper potential limits (UPLs): 0.9, 1.2, and 1.5 V_{RHE}. Information that can be extracted from these measurements are: (i) the stability, which can be quickly assessed at several potentials, (ii) the onset potential where dissolution starts, and (iii) changes in the shape of dissolution profiles for alloys with increasing number of constituents. The second protocol was started with a potentiostatic hold at a moderately anodic potential (1.2 V_{RHE}) for 10 min, followed by a reductive hold at 0.05 V_{RHE} for 5 min. The main asset of this protocol is that dissolution events can be separated (anodic and cathodic dissolution can be clearly quantified) allowing to identify even the smallest changes in the dissolution rate. Additionally, anodic/cathodic dissolution can be tracked on a long timescale allowing the observation of a possible temporal evolution of dissolution features. Both protocols were designed in a way to span a wide potential window covering the typical operating range for oxygen evolution, oxygen reduction, small organic molecules (e.g., alcohols), and hydrogen oxidation reaction. To study the effect of pH on the dissolution characteristics, these electrochemical protocols were performed both in 0.1 M $HClO_4$ and in 0.05 M KOH. We showed in preceding studies[52,53] that the presence of reactive gases (e.g., O_2, CO) or various fuels (alcohols, formic acid, ammonia) can greatly influence the stability of noble metal alloy electrocatalysts. Still, the measurements discussed in the following provide a plethora of useful information. As a control experiment, the stability of each alloy constituent (i.e., sputtered Pt, Ru, Ir, Rh, Pd) was studied by applying identical electrochemical protocols. As an example, Figure 3 shows the dissolution profiles recorded for the thin films in 0.1 M $HClO_4$ electrolyte solution.

Before making a more detailed analysis of these results, we have to make a few notes. Due to the complexity of the investigated materials (multiple metals and alloys ranging from unary to quinary composition, acidic and alkaline media, etc.), (i) dissolution profiles only for pure Pt are presented (dissolution profiles for the other pure metals are located in the Figures S6–S10) and (ii) the emerged dissolution features and the trends in between acidic and alkaline media are not discussed extensively in the main text, but in the supplemental information (see Figures S6–S10 and additional description) along with a detailed discussion of the emerged dissolution features and their pH dependence for each pure metal. In this section, first, we will discuss the measurement results qualitatively, which is followed by a more in-depth, quantitative analysis.

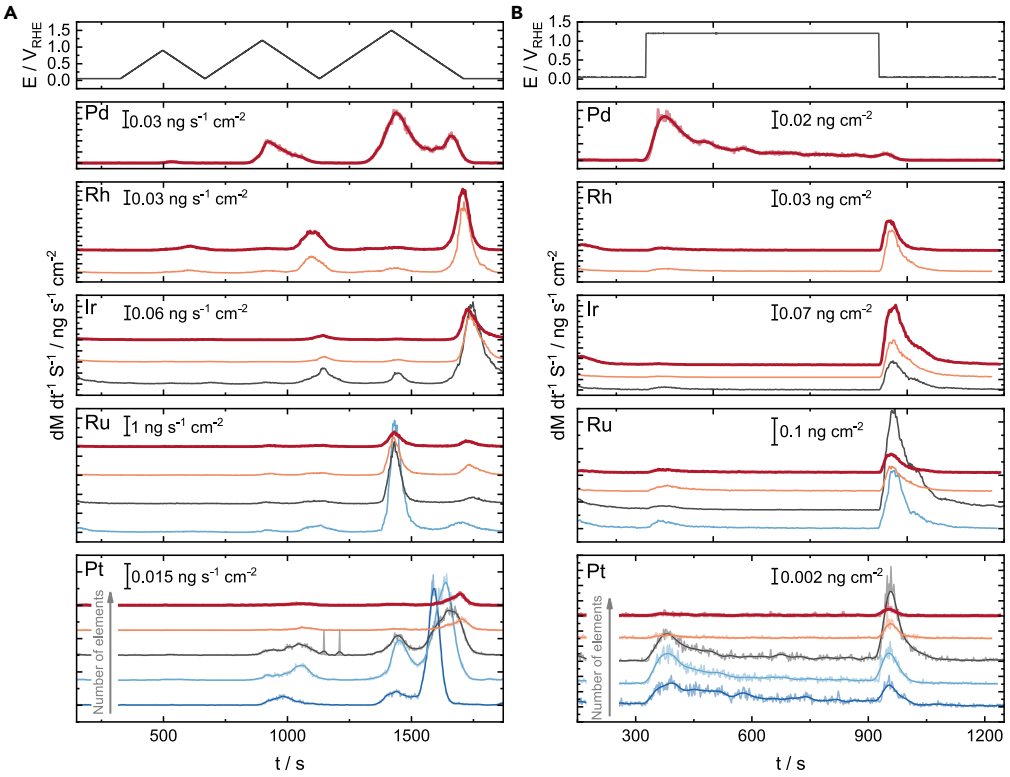

Figure 3. Dissolution profiles of the thin film samples in acidic electrolyte

(A) The protocol consisted of a 5 min hold at 0.05 V_{RHE}, followed by three consecutive CVs with gradually increasing upper potential limits (0.9, 1.2, and 1.5 V_{RHE}) applying a 5 mV s^{-1} scan rate. The protocol was finished with a 3 min potentiostatic hold at 0.05 V_{RHE}.

(B) The protocol started with a 5 min hold at 0.05 V_{RHE}, followed by an additional potentiostatic hold for 10 min at 1.2 V_{RHE}. The measurement was finished with a 5 min potentiostatic hold at 0.05 V_{RHE}. The electrolyte was 0.1 M $HClO_4$ in the case of both protocols and it was saturated with Ar during the measurements. In each panel, the dissolution profile at the bottom corresponds to either the pure metal (only for Pt) or to the alloy composed of the lowest number of elements. The topmost dissolution profile for each panel corresponds to the PtRuIrRhPd HEA sample (red, in bold). Dissolution curves were smoothed as needed using an FFT filter (points of window = 5–8). The original dataset is presented behind the smoothed profile with 50% transparency.

The first dissolution features were observed during the potentiostatic hold at 0.05 V_{RHE} prior to switching to the CVs (Figure 3A), which corresponds to the reduction of native oxides present on the surface of each metal or alloy electrocatalyst (data are not shown to simplify the curves).[54] Since the catalysts were stored under air in ambient conditions, the presence of such surface oxides is unavoidable. Moreover, the dissolution of these could be incomplete when the cell comes in contact with the electrocatalyst surface. An example of this is Ir, where the dissolution of the remaining native oxide layer only happened at the end of the first cycle (Figure S8A).

Pt dissolution notably increased for binary alloys (PtRu in this study and PtIr[31]) both in acidic (Figure 3) and alkaline (Figure S11) media. In 0.1 M $HClO_4$ both the anodic and cathodic dissolution peaks are affected. Contrastingly, higher anodic dissolution was only detected when the electrolyte was switched to 0.05 M KOH. Dissolution significantly decreased when the number of alloy constituents exceeded three, resulting in barely visible Pt dissolution features for PtRuIrRh and PtRuIrRhPd. A slightly different trend was seen for the potentiostatic holds; anodic dissolution remained constant/marginally increased, while cathodic dissolution became higher, especially for the ternary alloy in acidic electrolyte. In contrast, higher anodic dissolution was measured for PtRu and PtRuIr compared to Pt, while cathodic dissolution significantly decreased with the increasing number of alloying elements. As seen in the CVs, dissolution significantly decreased for alloys comprising four or five elements.

In contrast to Pt, *Ru* was stabilized already for the binary alloy (PtRu). Ru dissolution monotonically decreased with the addition of Ir, Rh, and Pd (Figures 3A and S11A). This was much more pronounced at alkaline pH, at which Ru is not stable if the applied potential exceeds 1.4 V_{RHE},[26] where alloying resulted in several orders of magnitude decrease in dissolution. Such trends for the potentiostatic holds can be only seen at alkaline pH (Figure S11B). While the data recorded in 0.1 M $HClO_4$ show that anodic dissolution decreases by alloying, the highest cathodic dissolution was observed for the ternary alloy.

No deviation from the decreasing trend can be identified for *Ir* either in acidic or alkaline electrolytes. This is especially true for the data recorded in 0.05 M KOH for the CV protocol (Figure S11A), where anodic dissolution peaks (at all UPLs) shrank, and cathodic dissolution peaks almost vanished. Additionally, when potentiostatic holds were applied, no dissolution features can be clearly identified if the number of alloying elements exceeded four, while both anodic and cathodic dissolution features are clearly recognizable for the ternary alloy (Figure S11B).

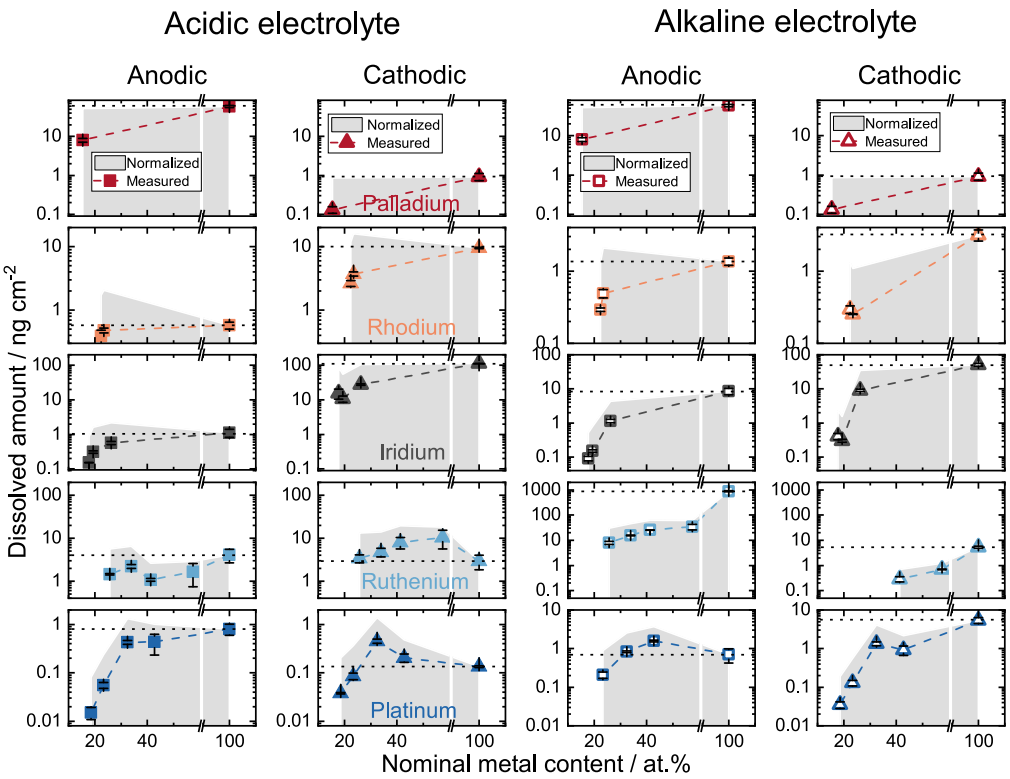

Figure 4. Dissolved amounts for each alloy constituent in the thin films in dependence of its content in the alloy

Left two columns (acidic, 0.1 M $HClO_4$ electrolyte): dissolved amounts as a function of the molar fraction of the given element in the alloy samples. Dissolved amounts were calculated by integrating the dissolution profiles presented in Figure 3B. Two columns on the right (alkaline, 0.05 M KOH electrolyte): dissolved amounts as the function of the molar fraction of the given element in the alloy samples. Dissolved amounts were calculated by integrating the dissolution profiles presented in Figure S11B. Filled and hollow triangles – dissolved amount of the given metal during the potentiostatic hold at 0.05 V_{RHE}, filled and hollow squares – dissolved amount of the given metal during the potentiostatic hold at 1.2 V_{RHE}. Dashed lines connecting the data points serve as a guide for the eye. The gray shaded area represents the normalized dissolved amounts determined by dividing the calculated dissolved amounts with the molar fraction of the given element in the given alloy. Nominal alloy composition was determined by XPS measurements. Error bars were calculated from at least two separate measurements; each was performed on a fresh catalyst spot.

In general, it is hard to talk about trends if the number of collected dissolution profiles in the given dataset is less than four. The only thing that can be done for *Rh* and *Pd* is to compare dissolution rates to their pure metal counterparts. Dissolution rates recorded for the *Rh*-containing alloys in alkaline electrolytes are lower compared to pure Rh. However, no clear differences can be identified between the quaternary and quinary compositions. Furthermore, the stability of Rh seems to be unaffected by alloying if experiments are carried out in acidic conditions.

A notably smaller *Pd* dissolution was recorded for the HEA sample compared to pure Pd regardless of the used electrolyte. The shape of the dissolution peaks is unaffected if the experiments were carried out in 0.1 M $HClO_4$. In contrast, cathodic and anodic dissolution peak ratios seem identical, and multiple small peaks can be observed in the CV protocol at 1.5 V_{RHE} UPL performed in 0.05 M KOH.

Interestingly, the onset potential of dissolution for each metal did not change visibly with the number of elements in the alloy.

As a next step, the qualitative observations discussed earlier were quantified by integrating all dissolution curves as follows: in the case of the CVs, dissolution that appeared during the entire cycle was integrated. For the sake of simplicity, only the dissolved amounts determined for the CVs with UPL = 1.2 and 1.5 V_{RHE} are presented in the following. Anodic and cathodic dissolution were integrated separately for the protocol consisting of potentiostatic holds. In addition to the integrated dissolution data, the *dissolved amounts were normalized (NDAs) by the molar fraction of the given element in each alloy as determined by XPS* (Figure 1B). Only mean dissolved amounts were included in these calculations. NDAs are represented as gray-shaded areas in each figure. The necessity of this normalization is addressed in the discussion and outlook section; here we only describe the observed trends.

Dissolved amounts determined for the potentiostatic holds performed in acidic media are presented in the left two columns in Figure 4. In contrast to the CVs (see Figure S12 and the corresponding discussion in the supplemental information), here we see the influence of alloying on cathodic and anodic dissolution separately. It is visible that based solely on dissolution, alloying had a similar effect on stability as in the case of the CVs; namely, both anodic and cathodic dissolution decreases with the decrease of the given metal amount in the alloy. However, Ru is an exception; anodic dissolution calculated for the HEA sample is only slightly smaller than the one determined for pure Ru, while

cathodic dissolution is identical for both samples. On the other hand, NDAs are either higher or similar to the ones calculated for the pure metals. The only exception is Pt, where the anodic NDA of the HEA sample is considerably smaller. In conclusion, the dissolved amounts for each metal visibly decreased with the decrease of the given metal in the alloy, but this decrease was not reflected in the NDA values.

Dissolved amounts calculated for the protocols performed in alkaline media are presented in two columns on the right in Figures S12 and 4 (hollow symbols in both cases). Stability of *all metals* visibly increased by alloying, similar to the data measured in 0.1 M $HClO_4$. However, here the decrease in dissolution is more evident. This is most notable for Pt and Ru dissolution calculated for the potentiostatic holds (hollow symbols in Figure 4), where no anodic dissolution features of Pt could be identified for the HEA sample. The same goes for the cathodic dissolution features of Ru in the case of the quaternary and quinary alloys. In contrast to the data recorded in acidic electrolytes, NDAs follow a similar trend for the CVs and the holds when the measurements were conducted in alkaline media. In general, NDAs show a steady decrease for Pt, Ru, and Ir with the increasing number of alloying elements. Ru stands out even from this line: NDA of Ru if *UPL* = 1.5 V_{RHE} dropped by two orders of magnitudes, while normalized anodic dissolution of Ru decreased by one order of magnitude for the PtRu samples compared to pure Ru. Elsewhere, identical effects on Ru dissolution were already observed when Ru or RuO_2 were alloyed with Ir (or IrO_2) notably decreasing the amount of dissolved Ru.[55,56] Similar to the acidic electrolyte case, NDA of Rh is slightly higher for the HEA sample than the one calculated for the pure Rh electrode. Finally, the normalized Pd dissolution of the HEA sample is almost identical to the value derived for pure Pd.

In summary, the dissolved amounts for each metal (especially for Ru) seem to scale with the amount of the given metal in the alloys. In contrast to the results obtained in acidic electrolytes, NDAs of Pt, Ru, and Ir show a steady decrease with their amount in the alloys, while alloying of Rh notably increased its NDA value. The NDA of Pd was not affected by the alloy formation—just like in the case of the acidic electrolyte.

Comparison of stability between thin films and carbon-supported NPs

While thin films are excellent model systems, in technical devices (e.g., fuel cells or electrolyzers) usually NPs are used as electrocatalysts, mostly either as unsupported NPs, or as carbon-supported NPs that are spray-coated on some sort of conductive substrate (e.g., carbon paper, titanium frit, etc.).[57] To spray-coat catalysts, homogeneous ink suspensions have to be prepared containing an ionomer and water/alcohol in a specific ratio. These are all additional materials that might positively or negatively affect the stability of the system and that are not present in the case of the thin films.[58] Therefore, the following questions arise: is the stability of the carbon-supported alloy NPs comparable to the stability determined for the model systems? Are any of the dissolution features altered? How does the stability of the carbon-supported NPs depend on circumstances such as electrolyte anions, pH, etc.? It was shown in the literature that corrosion of alloys can proceed via altered pathways based on the size of the NPs, which can result in different morphologies.[59,60] To answer these questions, the stability of carbon-supported alloy NPs was investigated. As it has been shown in the "physical and morphological characterization section", the composition of each NP system was similar to the sputtered films (equimolar composition); the metal loading was kept at 20 wt % uniformly. All performed electrochemical protocols are identical to those carried out for the thin film samples.

Results in acidic and alkaline electrolytes obtained by performing the protocol containing the potentiostatic holds are presented in Figures 5A and S13A. By taking a look at the dissolution profiles of NPs in Figures 5A and S12A, the first and most notable difference compared to the data gathered for the thin films is that they contain significantly more noise. The reason could be either the detachment of a large number of NPs or "preferential dealloying" of the NPs upon applying electrochemical protocols. NP detachment usually manifests as a sharp spike on the ICP-MS data as it can be seen, for example, on the dissolution profile of Pt recorded for the ternary alloy in alkaline media (Figure 5A). Another telltale sign of detachment is that the onset potential of dissolution is identical for all alloy constituents. None of these signs apply to the data recorded for the carbon-supported NPs (onset potential of dissolution is different and the observed "noise" manifested as identical, flat peaks instead of sharp spikes); thus, detachment as the origin can be excluded. The measured dissolution rates for all elements in the NPs are visibly higher compared to the thin films. This is due to the higher surface area of the carbon-supported NPs as it was already seen for the CVs (see Figures 2 and S2). Besides the noisier data, only a few differences can be noted. Cathodic Pt dissolution in 0.1 M $HClO_4$ is barely visible while it was clearly recognized in the case of the thin films. Contrastingly, the anodic dissolution of Rh is significantly higher for the carbon-supported NPs. In alkaline media, the cathodic dissolution in the case of Pt is the highest for the PtRu/C sample. Additionally, the cathodic dissolution peak is higher in the case of the PtRuIrRh/C sample. Besides these differences, dissolution profiles and trends are similar to those observed for the thin films. In the following, dissolution profiles were integrated, and the resulting dissolved amounts were plotted as the function of the molar fraction of each metal in the given alloy (Figures 5B, S13B, and S13C). Since here we do not have any of the pure metals in a nanocarbon-supported form, except for Pt, NDAs were calculated only for Pt. Error bars are relatively large due to the uncertainty introduced by the noisy dataset. It is visible that Pt, Ru, and Ir dissolution gradually decreases with the amount of the metals in the alloy both in acidic and alkaline media. The drop in dissolution is notably higher for the data recorded in 0.05 M KOH. Rh dissolution also decreases between the quaternary and quinary alloy samples. In contrast to the NDAs of Pt calculated for the thin films, here Pt NDA values for all the NP samples are either a bit higher or similar to the one calculated for the pure Pt/C sample.

Results gathered by performing the three CVs are presented in Figures S14A and S15A. The dataset is even noisier than it was for the potentiostatic holds. This is sometimes so severe that it makes it hard to clearly identify and separate the emerged dissolution features (e.g., Pt dissolution recorded for the PtRu/C sample both in acidic and alkaline electrolytes, Figures S14A and S15A). The onset potentials of dissolution and the shape of most dissolution peaks are close to the ones measured for the thin films. While dissolution features and trends of Ru dissolution are similar to those of the thin films in acidic media, besides anodic dissolution, we can observe a significant cathodic Ru

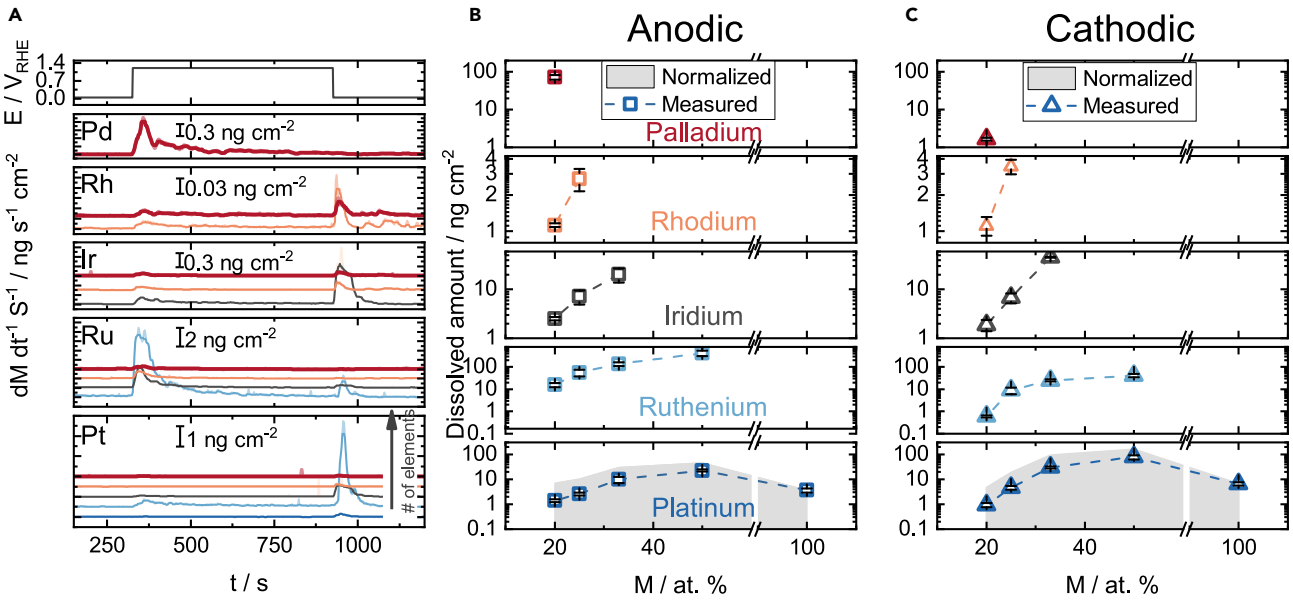

Figure 5. Dissolution profiles recorded for the carbon-supported alloy nanoparticles in alkaline media and calculated dissolved amounts as a function of the molar fraction of each metal in the alloy samples

(A) The protocol started with a 5 min hold at 0.05 V_{RHE}, which was followed by an additional potentiostatic hold for 10 min at 1.2 V_{RHE}. The measurement was finished with a 5 min potentiostatic hold at 0.05 V_{RHE}. The electrolyte was 0.05 M KOH in the case of both protocols and it was saturated with Ar during the measurements. In each panel, the dissolution profile at the bottom corresponds to either the pure metal (only Pt is included here) or to the alloy composed of the lowest number of elements. The topmost dissolution profile for each element corresponds to the HEA sample PtRuIrRhPd (red, in bold). Dissolution profiles were smoothed using an FFT filter (points of window = 5–8). The original dataset is presented behind the smoothed profile with 50% transparency.

(B and C) Dissolved amounts in dependence of the molar fraction of the given element in the alloy samples. Dissolved amounts were calculated by integrating the dissolution profiles presented in (A) (0.05 M KOH electrolyte). Squares – dissolved amount of the given metal during the potentiostatic hold at 1.2 V_{RHE}, Triangles – dissolved amount of the given metal during the potentiostatic hold at 0.05 V_{RHE}. The gray shaded area represents the normalized dissolved amounts determined by dividing the calculated dissolved amounts with the molar fraction of the given element in the given alloy. Error bars were calculated from at least two separate measurements; each was performed on a fresh catalyst spot.

dissolution for the PtRu/C and PtRuIr/C NPs in alkaline electrolytes. Cathodic Ir dissolution in 0.05 M KOH is also higher for the PtRuIr/C sample compared to its thin film counterpart. Finally, also at alkaline pH, only one (very noisy) dissolution peak can be identified for Rh instead of the previously observed cathodic and anodic dissolution. The trend in terms of dissolved amounts (Figures S14, S15B, and S15C) is identical to the one determined for the carbon-supported samples performing the potentiostatic holds. More importantly, it is also similar to trends observed for the thin films. However, all NDAs calculated for Pt in the alloy samples exceed the values of pure Pt. This difference can be explained by the difference in data quality: the statistical uncertainty introduced by the noisy data might mask the small gain (in this context it means that NDA values for the quinary alloy are smaller compared to the one determined for the pure metal(s)) in terms of NDAs we saw for the thin films.

To summarize, the stability of the carbon-supported NP systems and the thin films is comparable. Only small differences were observed between the dissolution features. The dissolved amounts of the NPs follow the same trends as in the case of the thin films regardless of the used electrolyte; namely, they scale with the amount of the given metal in the alloys. However, the measured data are visibly noisier for the carbon-supported NPs, which might hide the subtle differences. This might lead to a limited understanding of the behavior of the given system. Based on this, we recommend using well-defined model systems for systematic fundamental studies along with model material libraries to screen wide compositional ranges. When the behavior of the given catalyst is fully mapped, then one can move on to study systems that are specifically being characterized for use in real applications.

DISCUSSION AND OUTLOOK

In the past decades, one had to rely on the Pourbaix atlas to estimate the potential window in which the tested electrocatalyst is stable at a specific pH value.[61] Thermodynamic data combined with the E vs. pH diagrams allow locating the thermodynamically stable solid, aqueous, and gaseous species in the given potential window at a given pH. However, no significant progress has been made in the past 50 years to better understand certain regions on these diagrams (question marks on the diagrams, e.g., Pt, Pd, Ir, etc.). Additionally, while certain systems are extensively researched (e.g., Pt), others are only scarcely reported (e.g., Rh). Finally, the validity of parts of the original thermodynamic data is debated.[62] Furthermore, thermodynamics is only one side of the story; e.g., a metal that is thermodynamically stable at given conditions

(potential and pH) can still dissolve and vice versa. This means that contributions from kinetics and non-equilibrium transient processes are at least as important as thermodynamics. However, Pourbaix diagrams provide no insights in this regard.

In the past century, dissolution has been primarily examined in the context of corrosion. Most studies focused on engineering alloys (e.g., stainless steels with its main constituent Fe), and the goal was to investigate the effect of environmental conditions (such as the presence of moisture or seawater at the surface of the alloy) and various additives (e.g., additional metals in small concentrations) on corrosion properties.[63–66] Theoretical investigations had similar aims; numerous works were published that aimed to explain selective oxidation and dissolution (i.e., dealloying)[25,67] and the subsequently evolving nanoporosity,[68] determining critical alloy compositions (from which the dissolution kinetics of one component is determined by another component),[67] critical potentials (above which dissolution may proceed at high rate),[69] surface passivation,[69,70] and even modeling of anodic polarization curves,[63,71] etc. The common problem in these early studies is that i) none of them were performed under conditions occurring in electrocatalytic processes (electrolyte composition and pH, potential window, etc.), ii) most of the studies scrutinized bimetallic systems at best (alloys containing additional constituents were also studied, but in most cases, the given alloy consisted of two major constituents), and iii) only a few distinct compositions were investigated instead of the entire composition space.

In the last decade new *in situ* experimental tools were developed[43,45] along with the considerable evolution of materials characterization tools[59] giving an unprecedented chance to screen multinary electrocatalysts and understand the factors affecting their stability. A substantial amount of experimental data and understanding accumulated regarding the potential-resolved dissolution of transition metal and transition metal alloy electrodes.[28] We recently confirmed a clear correlation between intrinsic metal properties such as M-M and M-O bond energies and the amount of the dissolved metal.[28] Under oxidation, oxygen atoms are incorporated into the crystal lattice which leads to the breaking of M-M bonds. If the energy demand of this process is small, the dissolution tendency increases through the formation and dissolution of the formed undercoordinated metal sites. Under reduction, the amount of the formed oxide will determine dissolution (depending on both the M-M and M-O bond strength) and the rate of its reduction. These findings can be used as a starting point for predicting the dissolution stability of multinary material systems.

Since it is not possible to provide a detailed mechanistic picture of HEAs dissolution at this point, we focus our discussion on the main question of this work—"are HEAs more stable than single elements and traditional alloys containing less than five elements?" To see if configurational entropy plays a key role in the stability of HEAs, the term "normalized dissolved amount" (NDA) was introduced. The normalization was performed with the molar fraction of each element in the alloy determined by XPS. Based on this, a given sample shows improved stability if the NDA value is smaller than the one measured for the pure metal. According to our results presented in Figures 4 and S12, we conclude that in acidic media, anodic and cathodic dissolution decreased with the increasing number of alloy constituents. This is due to the gradually decreasing molar fraction of all metals with the increasing number of constituents in an alloy, rather than because of enhanced stability. Contrastingly, in alkaline media, NDAs for the HEA sample are significantly lower for Pt, Ru, and Ir, while no improvement was observed for Rh and Pd. Due to the lack of single-metal NPs, we were only able to calculate NDAs for Pt in the case of the carbon-supported NPs. However, the observed trends are similar to the ones determined for the thin films; thus, our conclusions can be applied to films and NPs. The difference between acidic and alkaline environments is very interesting but cannot be explained currently. Even though improved stability was observed for certain metals in the HEA sample under alkaline conditions, the improvement is not striking (gradually smaller dissolution was observed for all multinary alloys by the increasing number of alloy constituents). The decrease in dissolution can be rather explained by the relative amounts of elements in the given alloy instead of the synergistic effect of configurational entropy.

Does this mean that there is no effect of thermodynamic contributions on the stability of HEAs? Not necessarily. First of all, HEAs are complex systems where the interplay of at least five different metals determines their global stability. The electrochemical dissolution of even single metals is a complex process, depending on potential and electrode prehistory. Generally, the surface of an electrocatalyst is a dynamically evolving chemical environment where the given electrocatalytic reaction progresses in parallel with the transient dissolution of metal ions along with the formation of surface oxides and/or passivation layers.[30,54,72] This means that the surface composition changes instantaneously; thus, it is very hard (impossible at this point) to make valid predictions even for binary systems. In addition to this, ions present in the electrolyte along with the substrates and the formed (reactive) intermediates (e.g., CO) and products can (ir)reversibly adsorb at the electrode surface further complicating the observed dissolution phenomena.[53,72]

Based on our results it seems that all the effects described earlier overcompensated the thermodynamic contributions to the stability of the HEA samples. We were able to determine stability descriptors for single metals from the d block, but we do not know how these descriptors will be altered in the case of HEAs that contain five or more elements. Critical alloy compositions were determined for a handful of binary systems such as PtIr and PtRu, but it was only possible when the entire composition range was studied.[31] To deconvolute the effect of each metal in the transient dissolution process and to establish a general model concerning the corrosion of HEAs, substantial amounts of experimental data must be accumulated in the future. Additionally, we must note that in our study we only investigated the stability of one HEA, PtRuIrRhPd, where the molar fraction of each constituent was 20%. Therefore, our conclusions only apply to this system containing exactly these metals. It might easily be that a different composition (consisting mainly of metals showing higher stability) would show significantly improved stability compared to its pure metal counterparts. Still, we feel that there are several aspects/findings of our study that are immensely useful to studying the stability of other multimetallic alloys/HEAs.

- Claims regarding HEA stability are only valid if the stability of these systems is carefully studied under electrocatalytic conditions (pH, electrolyte composition, absence/presence of oxidizable substances, potential window, etc.) mimicking their future application.

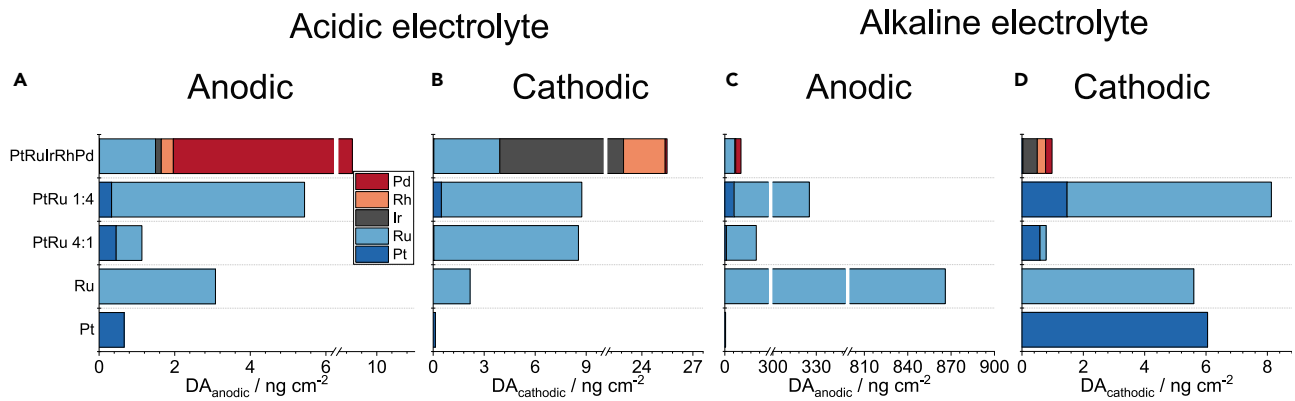

Figure 6. Dissolved amounts determined for various thin films: pure metals, binary, and high-entropy alloys

(A–D) Dissolved amounts calculated for the (A) anodic and (B) cathodic dissolution features recorded for pure Pt, Ru, bimetallic PtRu (1:4 and 4:1 elemental ratio), and for the PtRuIrRhPd HEA sample (0.1 M $HClO_4$ electrolyte). Dissolved amounts calculated for the (C) anodic and (D) cathodic dissolution features measured for pure Pt, Ru, bimetallic PtRu (1:4 and 4:1 elemental ratio), and for the PtRuIrRhPd HEA sample (0.05 M KOH electrolyte).

- It is not always enough to study the stability of model thin films; it has to be validated if findings can be transferred to samples that are closer to real-life applications (i.e., carbon-supported NPs).
- The amount of dissolved metals should be normalized by the molar fraction of each element in the alloy to resolve whether the change in stability occurred due to the decrease of the amount of metal (compared to the unary composition) or because of an additional stabilization phenomenon (be it thermodynamic or kinetic).
- On-line ICP-MS is a technique that can measure the amount of dissolved metal ions even for HEA samples, and because of its integrability in closed-loop autonomous workflows, it is still going to be the state-of-the-art method for this purpose.

To illustrate the effect of alloy composition on NDA, we performed the electrochemical protocol containing potentiostatic holds (5 min hold at 0.05 V_{RHE}, which was followed by an additional potentiostatic hold for 10 min at 1.2 V_{RHE}, the measurement was finished with a 5 min potentiostatic hold at 0.05 V_{RHE}) using a Pt-rich (Pt:Ru 4:1) and a Ru-rich (Pt:Ru 1:4) alloy thin film as working electrodes (Figure 6). In both cases, the lowest metal content in the alloys is 20 at%, i.e., the same as in the HEAs. We performed the protocol both in 0.1 M $HClO_4$ and in 0.05 M KOH. There are several important observations that can be made by analyzing these figures: i) the highest cumulative dissolution was measured for the HEA sample in acid, ii) cumulative dissolution is significantly higher for the Ru-rich binary alloy than the Pt-rich alloy regardless of the chemical environment, and iii) cumulative dissolution of the HEA sample is comparable to the one obtained for the Pt-rich binary alloy in alkaline media. The most important message is that by regulating the amount of the element with relatively higher stability (here: Pt) we were able to tune the stability of the resulting alloy. Moreover, it could be that only one or two elements are active toward the given electrocatalytic reaction instead of all alloy constituents. Therefore, activity and stability data must be interpreted together to find an optimal composition and to rule out elements that are inactive. This approach could lead to the discovery of electrocatalysts with high activity and stability. However, algorithms predicting the stability of promising electrocatalyst candidates are yet to come; thus, coupled experimental techniques (such as on-line ICP-MS of thin film libraries) will play a pivotal role in the future. While the composition space of, e.g., binary systems can be explored relatively easily, complexity in terms of the number of samples and experimental parameters increases tremendously for multinary systems. Because of this, the analysis of HEA material libraries can and will be only done by utilizing high-throughput methods and, most importantly, autonomous workflows.[73] Our on-line ICP-MS setup recently became capable of simultaneously screening the activity and stability of material libraries in a high-throughput manner.[44] In fact, HEAs are perfect model systems to develop these approaches further.[74,75] For example, the number of experiments can be considerably decreased by shifting from heuristic to Bayesian approaches (e.g., genetic algorithms).[76] By accumulating a substantial amount of experimental data, theoretical models will become more and more refined eventually leading to a future where the prediction of the activity and stability of multinary electrocatalyst such as HEAs is the reality.

Limitations of the study

The main limitation of our study is that instead of exploring the whole composition space, stability of only the equimolar compositions was investigated. The reason behind this was that our project was done in a traditional experimental workflow without the employment of any high-throughput/autonomous workflow tools. Because of this, and to keep the amount of recorded data manageable, we had to be selective regarding the pool of samples, especially since we wanted to compare sputtered thin films and carbon-supported NPs. Equimolar compositions were selected because, in theory, thermodynamic contributions are the highest in the case of these materials; hence, these should bear with the highest stability. While only a few compositions were tested, *general lessons learned from our study and summarized in four points under the "discussion and outlook" section are immensely useful for the scientific community dealing with the synthesis and application of multimetallic/HEAs in electrocatalytic reactions.* Our future effort will focus on performing similar experiments in an autonomous workflow by

integrating several elements of the high-throughput toolkit in our on-line ICP-MS setup allowing us to rapidly screen the entire composition space of multimetallic alloys.

STAR★METHODS

Detailed methods are provided in the online version of this paper and include the following:

- KEY RESOURCES TABLE
- RESOURCE AVAILABILITY
  - Lead contact
  - Materials availability
  - Data and code availability
- METHOD DETAILS
  - Synthesis of the electrocatalyst thin films
  - Synthesis of the carbon-supported nanoparticle electrocatalysts by carbothermal shock synthesis
  - Structural and morphological characterization
  - Rotating disk electrode (RDE) measurements
  - On-line ICP-MS measurements
- QUANTIFICATION AND STATISTICAL ANALYSIS

SUPPLEMENTAL INFORMATION

Supplemental information can be found online at https://doi.org/10.1016/j.isci.2023.107775.

ACKNOWLEDGMENTS

This work was partially funded by the Bavarian Ministry of Economic Affairs, Regional Development and Energy. A.K. acknowledges the financial support from the János Bolyai Research Scholarship of the Hungarian Academy of Sciences. L.H. acknowledges the support from the University of Maryland A. James Clark School of Engineering. B.X., A.S., and A.L. acknowledge funding from the DFG within the project LU1175/26-1.

AUTHOR CONTRIBUTIONS

Conceptualization: A.K. and S.C. Design of electrochemical experiments: A.K. and S.C., Synthesis of sputtered thin films and EDX measurements: B. X. and A. S. XPS measurements: K.J. Synthesis of carbon-supported NPs and TEM measurements: Q.D. and T.L. HAADF-STEM and spectrum imaging: A.Kö. and A.H. AFM measurements and data analysis: T.B. Original draft: A.K. Revision and editing of the original draft: S.C., L.H., A.L., Q.D., B.X., A.S., K.J., T.B., T.P., A.Kö., and A.H. Supervision of experimental work: S.C.

DECLARATION OF INTERESTS

The authors declare no competing interests.

Received: August 4, 2023
Revised: August 16, 2023
Accepted: August 28, 2023
Published: August 30, 2023

REFERENCES

1. He, J., and Janáky, C. (2020). Recent Advances in Solar-Driven Carbon Dioxide Conversion: Expectations versus Reality. ACS Energy Lett. *5*, 1996–2014. https://doi.org/10.1021/acsenergylett.0c00645.
2. Cai, B., Henning, S., Herranz, J., Schmidt, T.J., and Eychmüller, A. (2017). Nanostructuring Noble Metals as Unsupported Electrocatalysts for Polymer Electrolyte Fuel Cells. Adv. Energy Mater. *7*, 1700548. https://doi.org/10.1002/aenm.201700548.
3. Speck, F.D., Ali, F.S.M., Paul, M.T.Y., Singh, R.K., Böhm, T., Hofer, A., Kasian, O., Thiele, S., Bachmann, J., Dekel, D.R., et al. (2020). Improved Hydrogen Oxidation Reaction Activity and Stability of Buried Metal-Oxide Electrocatalyst Interfaces. Chem. Mater. *32*, 7716–7724. https://doi.org/10.1021/acs.chemmater.0c02048.
4. Delmo, E.P., Wang, Y., Wang, J., Zhu, S., Li, T., Qin, X., Tian, Y., Zhao, Q., Jang, J., Wang, Y., et al. (2022). Metal organic framework-ionic liquid hybrid catalysts for the selective electrochemical reduction of CO_2 to CH_4. Chin. J. Catal. *43*, 1687–1696. https://doi.org/10.1016/s1872-2067(21)63970-0.
5. Löffler, T., Savan, A., Garzón-Manjón, A., Meischein, M., Scheu, C., Ludwig, A., and Schuhmann, W. (2019). Toward a Paradigm Shift in Electrocatalysis Using Complex Solid Solution Nanoparticles. ACS Energy Lett. *4*, 1206–1214. https://doi.org/10.1021/acsenergylett.9b00531.
6. Savage, N. (2021). High-entropy alloys expand their range. Nature *595*, S4–S5. https://doi.org/10.1038/d41586-021-01788-0.
7. Yeh, J.W., Chen, S.K., Lin, S.J., Gan, J.Y., Chin, T.S., Shun, T.T., Tsau, C.H., and Chang, S.Y. (2004). Nanostructured High-Entropy Alloys with Multiple Principal Elements: Novel Alloy Design Concepts and Outcomes. Adv. Eng. Mater. *6*, 299–303. https://doi.org/10.1002/adem.200300567.
8. Cantor, B., Chang, I.T.H., Knight, P., and Vincent, A.J.B. (2004). Microstructural development in equiatomic multicomponent

alloys. Mater. Sci. Eng. *375–377*, 213–218. https://doi.org/10.1016/j.msea.2003.10.257.
9. Yao, Y., Dong, Q., Brozena, A., Luo, J., Miao, J., Chi, M., Wang, C., Kevrekidis, I.G., Ren, Z.J., Greeley, J., et al. (2022). High-entropy nanoparticles: Synthesis-structure-property relationships and data-driven discovery. Science *376*, eabn3103. https://doi.org/10.1126/science.abn3103.
10. Sun, Y., and Dai, S. (2021). High-entropy materials for catalysis: A new frontier. Sci. Adv. *7*, eabg1600. https://doi.org/10.1126/sciadv.abg1600.
11. Yao, Y., Huang, Z., Xie, P., Lacey, S.D., Jacob, R.J., Xie, H., Chen, F., Nie, A., Pu, T., Rehwoldt, M., et al. (2018). Carbothermal shock synthesis of high-entropy-alloy nanoparticles. Science *359*, 1489–1494. https://doi.org/10.1126/science.aan5412.
12. Löffler, T., Ludwig, A., Rossmeisl, J., and Schuhmann, W. (2021). What Makes High-Entropy Alloys Exceptional Electrocatalysts? Angew. Chem. Int. Ed. Engl. *60*, 26894–26903. https://doi.org/10.1002/anie.202109212.
13. Pedersen, J.K., Batchelor, T.A., Yan, D., Skjegstad, L.E.J., and Rossmeisl, J. (2021). Surface electrocatalysis on high-entropy alloys. Curr. Opin. Electrochem. *26*, 100651. https://doi.org/10.1016/j.coelec.2020.100651.
14. Batchelor, T.A., Pedersen, J.K., Winther, S.H., Castelli, I.E., Jacobsen, K.W., and Rossmeisl, J. (2019). High-Entropy Alloys as a Discovery Platform for Electrocatalysis. Joule *3*, 834–845. https://doi.org/10.1016/j.joule.2018.12.015.
15. Wu, D., Kusada, K., Yamamoto, T., Toriyama, T., Matsumura, S., Kawaguchi, S., Kubota, Y., and Kitagawa, H. (2020). Platinum-Group-Metal High-Entropy-Alloy Nanoparticles. J. Am. Chem. Soc. *142*, 13833–13838. https://doi.org/10.1021/jacs.0c04807.
16. Li, S., Wang, J., Lin, X., Xie, G., Huang, Y., Liu, X., and Qiu, H.J. (2020). Flexible Solid-State Direct Ethanol Fuel Cell Catalyzed by Nanoporous High-Entropy Al-Pd-Ni-Cu-Mo Anode and Spinel $(AlMnCo)_3O_4$ Cathode. Adv. Funct. Mater. *31*, 2007129. https://doi.org/10.1002/adfm.202007129.
17. Anderson, B.D., and Tracy, J.B. (2014). Nanoparticle conversion chemistry: Kirkendall effect, galvanic exchange, and anion exchange. Nanoscale *6*, 12195–12216. https://doi.org/10.1039/c4nr02025a.
18. Sivanantham, A., Lee, H., Hwang, S.W., Ahn, B., and Cho, I.S. (2021). Preparation, electrical and electrochemical characterizations of CuCoNiFeMn high-entropy-alloy for overall water splitting at neutral-pH. J. Mater. Chem. A Mater. *9*, 16841–16851. https://doi.org/10.1039/d1ta02621f.
19. Sharma, L., Katiyar, N.K., Parui, A., Das, R., Kumar, R., Tiwary, C.S., Singh, A.K., Halder, A., and Biswas, K. (2021). Low-cost high entropy alloy (HEA) for high-efficiency oxygen evolution reaction (OER). Nano Res. *15*, 4799–4806. https://doi.org/10.1007/s12274-021-3802-4.
20. Yao, R.Q., Zhou, Y.T., Shi, H., Wan, W.B., Zhang, Q.H., Gu, L., Zhu, Y.F., Wen, Z., Lang, X.Y., and Jiang, Q. (2020). Nanoporous Surface High-Entropy Alloys as Highly Efficient Multisite Electrocatalysts for Nonacidic Hydrogen Evolution Reaction. Adv. Funct. Mater. *31*, 2009613. https://doi.org/10.1002/adfm.202009613.
21. Fereja, S.L., Zhang, Z., Fang, Z., Guo, J., Zhang, X., Liu, K., Li, Z., and Chen, W. (2022). High-Entropy Oxide Derived from Metal-Organic Framework as a Bifunctional Electrocatalyst for Efficient Urea Oxidation and Oxygen Evolution Reactions. ACS Appl. Mater. Interfaces *14*, 38727–38738. https://doi.org/10.1021/acsami.2c09161.
22. Vass, Á., Endrődi, B., Samu, G.F., Balog, Á., Kormányos, A., Cherevko, S., and Janáky, C. (2021). Local Chemical Environment Governs Anode Processes in CO_2 Electrolyzers. ACS Energy Lett. *6*, 3801–3808. https://doi.org/10.1021/acsenergylett.1c01937.
23. Nørskov, J.K., Rossmeisl, J., Logadottir, A., Lindqvist, L., Kitchin, J.R., Bligaard, T., and Jónsson, H. (2004). Origin of the Overpotential for Oxygen Reduction at a Fuel-Cell Cathode. J. Phys. Chem. B *108*, 17886–17892. https://doi.org/10.1021/jp047349j.
24. Banko, L., Krysiak, O.A., Pedersen, J.K., Xiao, B., Savan, A., Loffler, T., Baha, S., Rossmeisl, J., Schuhmann, W., and Ludwig, A. (2022). Unravelling Composition-Activity-Stability Trends in High Entropy Alloy Electrocatalysts by Using a Data-Guided Combinatorial Synthesis Strategy and Computational Modeling. Adv. Energy Mater. *12*. https://doi.org/10.1002/aenm.202103312.
25. Greeley, J., and Nørskov, J. (2007). Electrochemical dissolution of surface alloys in acids: Thermodynamic trends from first-principles calculations. Electrochim. Acta *52*, 5829–5836. https://doi.org/10.1016/j.electacta.2007.02.082.
26. Schalenbach, M., Kasian, O., Ledendecker, M., Speck, F.D., Mingers, A.M., Mayrhofer, K.J.J., and Cherevko, S. (2017). The Electrochemical Dissolution of Noble Metals in Alkaline Media. Electrocatalysis *9*, 153–161. https://doi.org/10.1007/s12678-017-0438-y.
27. Cherevko, S. (2018). Electrochemical Dissolution of Noble Metals (Elsevier Inc), pp. 69–75.
28. Speck, F.D., Zagalskaya, A., Alexandrov, V., and Cherevko, S. (2021). Periodicity in the Electrochemical Dissolution of Transition Metals. Angew. Chem., Int. Ed. Engl. *60*, 13343–13349. https://doi.org/10.1002/anie.202100337.
29. Vijh, A.K., and Bélanger, G. (1976). The anodic dissolution rates of noble metals in relation to their solid state cohesion. Corrosion Sci. *16*, 869–872. https://doi.org/10.1016/0010-938x(76)90016-0.
30. Bogar, M., Yakovlev, Y., Sandbeck, D.J.S., Cherevko, S., Matolínová, I., Amenitsch, H., and Khalakhan, I. (2021). Interplay Among Dealloying, Ostwald Ripening, and Coalescence in Pt_XNi_{100-X} Bimetallic Alloys under Fuel-Cell-Related Conditions. ACS Catal. *11*, 11360–11370. https://doi.org/10.1021/acscatal.1c01111.
31. Kormányos, A., Savan, A., Ludwig, A., Speck, F.D., Mayrhofer, K.J., and Cherevko, S. (2021). Electrocatalytic oxidation of 2-propanol on Pt_xIr_{100-x} bifunctional electrocatalysts – A thin-film materials library study. J. Catal. *396*, 387–394. https://doi.org/10.1016/j.jcat.2021.02.021.
32. George, M., Zhang, G.R., Schmitt, N., Brunnengräber, K., Sandbeck, D.J.S., Mayrhofer, K.J.J., Cherevko, S., and Etzold, B.J.M. (2019). Effect of Ionic Liquid Modification on the ORR Performance and Degradation Mechanism of Trimetallic PtNiMo/C Catalysts. ACS Catal. *9*, 8682–8692. https://doi.org/10.1021/acscatal.9b01772.
33. Polani, S., MacArthur, K.E., Klingenhof, M., Wang, X., Paciok, P., Pan, L., Feng, Q., Kormányos, A., Cherevko, S., Heggen, M., and Strasser, P. (2021). Size and Composition Dependence of Oxygen Reduction Reaction Catalytic Activities of Mo-Doped PtNi/C Octahedral Nanocrystals. ACS Catal. *11*, 11407–11415. https://doi.org/10.1021/acscatal.1c01761.
34. Yusenko, K.V., Riva, S., Carvalho, P.A., Yusenko, M.V., Arnaboldi, S., Sukhikh, A.S., Hanfland, M., and Gromilov, S.A. (2017). First hexagonal close packed high-entropy alloy with outstanding stability under extreme conditions and electrocatalytic activity for methanol oxidation. Scripta Mater. *138*, 22–27. https://doi.org/10.1016/j.scriptamat.2017.05.022.
35. Wang, A.-L., Wan, H.-C., Xu, H., Tong, Y.-X., and Li, G.-R. (2014). Quinary PdNiCoCuFe Alloy Nanotube Arrays as Efficient Electrocatalysts for Methanol Oxidation. Electrochim. Acta *127*, 448–453. https://doi.org/10.1016/j.electacta.2014.02.076.
36. Li, H., Han, Y., Zhao, H., Qi, W., Zhang, D., Yu, Y., Cai, W., Li, S., Lai, J., Huang, B., and Wang, L. (2020). Fast site-to-site electron transfer of high-entropy alloy nanocatalyst driving redox electrocatalysis. Nat. Commun. *11*, 5437. https://doi.org/10.1038/s41467-020-19277-9.
37. Löffler, T., Waag, F., Gökce, B., Ludwig, A., Barcikowski, S., and Schuhmann, W. (2021). Comparing the Activity of Complex Solid Solution Electrocatalysts Using Inflection Points of Voltammetric Activity Curves as Activity Descriptors. ACS Catal. *11*, 1014–1023. https://doi.org/10.1021/acscatal.0c03313.
38. Nellaiappan, S., Katiyar, N.K., Kumar, R., Parui, A., Malviya, K.D., Pradeep, K.G., Singh, A.K., Sharma, S., Tiwary, C.S., and Biswas, K. (2020). High-Entropy Alloys as Catalysts for the CO_2 and CO Reduction Reactions: Experimental Realization. ACS Catal. *10*, 3658–3663. https://doi.org/10.1021/acscatal.9b04302.
39. McCrory, C.C.L., Jung, S., Peters, J.C., and Jaramillo, T.F. (2013). Benchmarking heterogeneous electrocatalysts for the oxygen evolution reaction. J. Am. Chem. Soc. *135*, 16977–16987. https://doi.org/10.1021/ja407115p.
40. Wei, C., Rao, R.R., Peng, J., Huang, B., Stephens, I.E.L., Risch, M., Xu, Z.J., and Shao-Horn, Y. (2019). Recommended Practices and Benchmark Activity for Hydrogen and Oxygen Electrocatalysis in Water Splitting and Fuel Cells. Adv. Mater. *31*, e1806296. https://doi.org/10.1002/adma.201806296.
41. Chung, D.Y., Yoo, J.M., and Sung, Y.E. (2018). Highly Durable and Active Pt-Based Nanoscale Design for Fuel-Cell Oxygen-Reduction Electrocatalysts. Adv. Mater. *30*, e1704123. https://doi.org/10.1002/adma.201704123.
42. Wang, L., Gao, W., Liu, Z., Zeng, Z., Liu, Y., Giroux, M., Chi, M., Wang, G., Greeley, J., Pan, X., and Wang, C. (2017). Core–Shell Nanostructured Cobalt–Platinum Electrocatalysts with Enhanced Durability. ACS Catal. *8*, 35–42. https://doi.org/10.1021/acscatal.7b02501.
43. Jenewein, K.J., Kormányos, A., Knöppel, J., Mayrhofer, K.J.J., and Cherevko, S. (2021). Accessing In Situ Photocorrosion under Realistic Light Conditions: Photoelectrochemical Scanning Flow Cell Coupled to Online ICP-MS. ACS Meas. Sci. Au *1*, 74–81. https://doi.org/10.1021/acsmeasuresciau.1c00016.

44. Jenewein, K.J., Akkoc, G.D., Kormányos, A., and Cherevko, S. (2022). Automated high-throughput activity and stability screening of electrocatalysts. Chem Catal. *2*, 2778–2794. https://doi.org/10.1016/j.checat.2022.09.019.
45. Kasian, O., Geiger, S., Mayrhofer, K.J.J., and Cherevko, S. (2019). Electrochemical On-line ICP-MS in Electrocatalysis Research. Chem. Rec. *19*, 2130–2142. https://doi.org/10.1002/tcr.201800162.
46. Batchelor, T.A.A., Löffler, T., Xiao, B., Krysiak, O.A., Strotkötter, V., Pedersen, J.K., Clausen, C.M., Savan, A., Li, Y., Schuhmann, W., et al. (2021). Complex-Solid-Solution Electrocatalyst Discovery by Computational Prediction and High-Throughput Experimentation. Angew. Chem., Int. Ed. Engl. *60*, 6932–6937. https://doi.org/10.1002/anie.202014374.
47. Yao, Y., Huang, Z., Hughes, L.A., Gao, J., Li, T., Morris, D., Zeltmann, S.E., Savitzky, B.H., Ophus, C., Finfrock, Y.Z., et al. (2021). Extreme mixing in nanoscale transition metal alloys. Matter *4*, 2340–2353. https://doi.org/10.1016/j.matt.2021.04.014.
48. Cherevko, S., Zeradjanin, A.R., Topalov, A.A., Kulyk, N., Katsounaros, I., and Mayrhofer, K.J.J. (2014). Dissolution of Noble Metals during Oxygen Evolution in Acidic Media. ChemCatChem *6*, 2219–2223. https://doi.org/10.1002/cctc.201402194.
49. Li, T., Yao, Y., Ko, B.H., Huang, Z., Dong, Q., Gao, J., Chen, W., Li, J., Li, S., Wang, X., et al. (2021). Carbon-Supported High-Entropy Oxide Nanoparticles as Stable Electrocatalysts for Oxygen Reduction Reactions. Adv. Funct. Mater. *31*. https://doi.org/10.1002/adfm.202010561.
50. Breiter, M. (1962). Über die art der wasserstoffadsorption an platinmetallelektroden. Electrochim. Acta *7*, 25–38. https://doi.org/10.1016/0013-4686(62)80014-0.
51. Will, F.G. (1965). Hydrogen Adsorption on Platinum Single Crystal Electrodes. J. Electrochem. Soc. *112*, 451. https://doi.org/10.1149/1.2423567.
52. Pizzutilo, E., Freakley, S.J., Geiger, S., Baldizzone, C., Mingers, A., Hutchings, G.J., Mayrhofer, K.J.J., and Cherevko, S. (2017). Addressing stability challenges of using bimetallic electrocatalysts: the case of gold–palladium nanoalloys. Catal. Sci. Technol. *7*, 1848–1856. https://doi.org/10.1039/c7cy00291b.
53. Kormányos, A., Speck, F.D., Mayrhofer, K.J.J., and Cherevko, S. (2020). Influence of Fuels and pH on the Dissolution Stability of Bifunctional PtRu/C Alloy Electrocatalysts. ACS Catal. *10*, 10858–10870. https://doi.org/10.1021/acscatal.0c02094.
54. Cherevko, S. (2017). Electrochemical dissolution of noble metals native oxides. J. Electroanal. Chem. *787*, 11–13. https://doi.org/10.1016/j.jelechem.2017.01.029.
55. Escalera-López, D., Czioska, S., Geppert, J., Boubnov, A., Röse, P., Saraçi, E., Krewer, U., Grunwaldt, J.-D., and Cherevko, S. (2021). Phase- and Surface Composition-Dependent Electrochemical Stability of Ir-Ru Nanoparticles during Oxygen Evolution Reaction. ACS Catal. *11*, 9300–9316. https://doi.org/10.1021/acscatal.1c01682.
56. Kasian, O., Geiger, S., Stock, P., Polymeros, G., Breitbach, B., Savan, A., Ludwig, A., Cherevko, S., and Mayrhofer, K.J.J. (2016). On the Origin of the Improved Ruthenium Stability in RuO2–IrO2Mixed Oxides. J. Electrochem. Soc. *163*, F3099–F3104. https://doi.org/10.1149/2.0131611jes.
57. Endrődi, B., Samu, A., Kecsenovity, E., Halmágyi, T., Sebők, D., and Janáky, C. (2021). Operando cathode activation with alkali metal cations for high current density operation of water-fed zero-gap carbon dioxide electrolyzers. Nat. Energy *6*, 439–448. https://doi.org/10.1038/s41560-021-00813-w.
58. Knöppel, J., Möckl, M., Escalera-López, D., Stojanovski, K., Bierling, M., Böhm, T., Thiele, S., Rzepka, M., and Cherevko, S. (2021). On the limitations in assessing stability of oxygen evolution catalysts using aqueous model electrochemical cells. Nat. Commun. *12*, 2231. https://doi.org/10.1038/s41467-021-22296-9.
59. Oezaslan, M., Heggen, M., and Strasser, P. (2012). Size-dependent morphology of dealloyed bimetallic catalysts: linking the nano to the macro scale. J. Am. Chem. Soc. *134*, 514–524. https://doi.org/10.1021/ja2088162.
60. Gan, L., Heggen, M., O'Malley, R., Theobald, B., and Strasser, P. (2013). Understanding and controlling nanoporosity formation for improving the stability of bimetallic fuel cell catalysts. Nano Lett. *13*, 1131–1138. https://doi.org/10.1021/nl304488q.
61. Pourbaix, M. (1974). Atlas of Electrochemical Equilibria in Aqueous Solutions.
62. Cherevko, S., Kulyk, N., and Mayrhofer, K.J. (2016). Durability of platinum-based fuel cell electrocatalysts: Dissolution of bulk and nanoscale platinum. Nano Energy *29*, 275–298. https://doi.org/10.1016/j.nanoen.2016.03.005.
63. Mueller, W.A. (1962). Derivation of Anodic Dissolution Curve Of Alloys from those of Metallic Components. Corrosion *18*, 73t–79t. https://doi.org/10.5006/0010-9312-18.2.73.
64. Pickering, H.W., and Wagner, C. (1967). Electrolytic Dissolution of Binary Alloys Containing a Noble Metal. J. Electrochem. Soc. *114*, 698. https://doi.org/10.1149/1.2426709.
65. Newman, R.C., and Sieradzki, K. (1994). Metallic corrosion. Science *263*, 1708–1709. https://doi.org/10.1126/science.263.5154.1708.
66. Han, K.N., and Fuerstenau, M.C. (2003). Dissolution behavior of metals from binary alloys. Int. J. Miner. Process. *72*, 355–364. https://doi.org/10.1016/s0301-7516(03)00110-8.
67. Popov, Y.A., Mouhammad, S., and Saha, S. (2000). A theory of the active dissolution of alloys. Prot. Met. *36*, 157–164. https://doi.org/10.1007/bf02758339.
68. Erlebacher, J., Aziz, M.J., Karma, A., Dimitrov, N., and Sieradzki, K. (2001). Evolution of nanoporosity in dealloying. Nature *410*, 450–453. https://doi.org/10.1038/35068529.
69. Landolt, D. (1990). Contributions of surface analysis to corrosion science: Selective dissolution and oxidation phenomena in alloy corrosion. Surf. Interface Anal. *15*, 395–404. https://doi.org/10.1002/sia.740150702.
70. Ateya, B.G., and Pickering, H.W. (1996). The effects of potential and kinetic parameters on the formation of passivating noble metal rich surface layers during the selective dissolution of binary alloys. Corrosion Sci. *38*, 1245–1267. https://doi.org/10.1016/0010-938x(96)00015-7.
71. Steigerwald, R.F., and Greene, N.D. (1962). The Anodic Dissolution of Binary Alloys. J. Electrochem. Soc. *109*, 1026. https://doi.org/10.1149/1.2425230.
72. Topalov, A.A., Zeradjanin, A.R., Cherevko, S., and Mayrhofer, K.J. (2014). The impact of dissolved reactive gases on platinum dissolution in acidic media. Electrochem. Commun. *40*, 49–53. https://doi.org/10.1016/j.elecom.2013.12.021.
73. Kormányos, A., Jenewein, K.J., and Cherevko, S. (2022). High-throughput workflows in the service of (photo) electrocatalysis research. Trends in Chemistry *4*, 475–478. https://doi.org/10.1016/j.trechm.2022.01.004.
74. Resasco, J., Abild-Pedersen, F., Hahn, C., Bao, Z., Koper, M.T.M., and Jaramillo, T.F. (2022). Enhancing the connection between computation and experiments in electrocatalysis. Nat. Catal. *5*, 374–381. https://doi.org/10.1038/s41929-022-00789-0.
75. Chen, Z.W., Chen, L., Gariepy, Z., Yao, X., and Singh, C.V. (2022). High-throughput and machine-learning accelerated design of high entropy alloy catalysts. Trends in Chemistry *4*, 577–579. https://doi.org/10.1016/j.trechm.2022.03.010.
76. Pedersen, J.K., Clausen, C.M., Krysiak, O.A., Xiao, B., Batchelor, T.A.A., Löffler, T., Mints, V.A., Banko, L., Arenz, M., Savan, A., et al. (2021). Bayesian Optimization of High-Entropy Alloy Compositions for Electrocatalytic Oxygen Reduction. Angew. Chem. *133*, 24346–24354. https://doi.org/10.1002/ange.202108116.
77. Klemm, S.O., Topalov, A.A., Laska, C.A., and Mayrhofer, K.J. (2011). Coupling of a high throughput microelectrochemical cell with online multielemental trace analysis by ICP-MS. Electrochem. Commun. *13*, 1533–1535. https://doi.org/10.1016/j.elecom.2011.10.017.

STAR★METHODS

KEY RESOURCES TABLE

REAGENT or RESOURCE	SOURCE	IDENTIFIER
Chemicals, peptides, and recombinant proteins		
Vulcan XC72 Carbon black	Cabot	https://www.cabotcorp.com/solutions/products-plus/carbon-blacks-for-elastomer-reinforcement/conductive
AvCarb MGL190 carbon paper	Fuel Cell Store	Cat# 1594008-2
$H_2PtCl_6{\cdot}xH_2O$	Sigma Aldrich	CAS# 13454-96-1
$RuCl_3{\cdot}xH_2O$	Sigma Aldrich	CAS# 14898-67-0
$IrCl_3{\cdot}xH_2O$	Sigma Aldrich	CAS# 10025-83-9
$RhCl_3{\cdot}xH_2O$	Sigma Aldrich	CAS# 10049-07-7
$PdCl_2$	Sigma Aldrich	CAS# 7647-10-1
Ethanol	Sigma Aldrich	CAS# 64-17-5
$HClO_4$ (70%, Suprapur®)	Merck	CAS# 7601-90-3
HNO3 (65%, Sprapur®)	Merck	CAS# 7697-37-2
KOH (99.995% trace metals basis)	Merck	CAS# 1310-58-3
Nafion (5wt %)	Merck	CAS# 31175-20-9
Isopropanol (ACS, 99.5+%)	VWR	CAS# 67-63-0
Ar (99.999%)	Air Liquide Deutschland GmbH	Cat# P0021S10R2A001
Pt Sputter target (99.99% purity)	Sindlhauser Materials GmbH	Artikel-Nr. 120835
Ru Sputter target (99.95% purity)	EvoChem GmbH	Batch: CA130730-0201
Ir Sputter target (99.9% purity)	EvoChem GmbH	CAS-Nr.: 7439-88-5
Rh Sputter target (99.9% purity)	FHR centrotherm group	Artikel-Nr.: 232954
Pd Sputter target (99.99% purity)	SenVac Thin film Technologies GmbH	(none)
Si (100) wafer (10 cm diameter)	MicroChemicals GmbH	WWD4 0525 250B 1314 S501 Lot: 25836
Ti sputter target (99.99% purity)	Goodfellow Cambridge Ltd.	LS 374938/2
Pt ICP standard (Certipur)	Merck	Cat# 1702190100
Re ICP standard (Certipur)	Merck	Cat# 1703440100
Ru ICP standard (Certipur)	Merck	Cat# 1703470100
Mo ICP standard (Certipur)	Merck	Cat# 1703340100
Ir ICP standard (Certipur)	Merck	Cat# 1703250100
Rh ICP standard (Certipur)	Merck	Cat# 1703450100
In ICP standard (Certipur)	Merck	Cat# 1703240100
Pd ICP standard (Certipur)	Merck	Cat# 1703390100
Te ICP standard (Certipur)	Merck	Cat# 1703570100

RESOURCE AVAILABILITY

Lead contact

Further information and requests should be directed to and will be fulfilled by the lead contact, Attila Kormányos (kormanyos.attila@szte.hu)

Materials availability

All materials generated in this study may be made available upon reasonable request.

Data and code availability

- Data reported in this study will be shared by the lead contact upon reasonable request.
- This paper does not report any original code.
- Any additional information required to reanalyze the data reported in this paper is available from the lead contact upon reasonable request.

METHOD DETAILS

Synthesis of the electrocatalyst thin films

Thin films were deposited using a loadlock-equipped ultra-high vacuum PVD machine (CMS 400/600 LIN, DCA instruments Finland). The deposition chamber has 5 magnetron sputter cathodes spaced 72° apart in a confocal, sputter-down arrangement. Elemental targets of Ir (purity 99.9%), Pd (purity 99.99%), Pt (purity 99.99%), Rh (purity 99.9%) and Ru (purity 99.5%) were used, with continuous rotation of the substrate leading to atomically-mixed films of uniform thickness. Prior to deposition, the chamber vacuum was about $2x10^{-6}$ Pa, and the targets were precleaned by sputtering against individual, closed shutters. Substrates were Ø100 single crystal (100) silicon wafers with a 500 nm wet thermal SiO_2 barrier layer against substrate reactions, and a 5 nm Ti (purity 99.9999%) adhesion layer sputter deposited immediately prior to the investigated thin films. Depositions were performed at 25°C without additional intentional heating, and a pressure of 0.67 Pa (Ar, 99.9999% purity, 60 sccm flow rate) with times adjusted to result in approximately 100 nm thick films, or 50 nm in the case of Pt, PtRu and PtRuIr. For multi-element films, the powers applied to each target were set to produce the desired alloy composition

Synthesis of the carbon-supported nanoparticle electrocatalysts by carbothermal shock synthesis

The precursor solution with 0.05 mol/L was prepared by dissolving the metal salt in ethanol. The various multielement solutions were obtained based on the designed elemental composition with an equimolar concentration for each element. The precursor solution was mixed with carbon black at a total metal loading of 20 wt %. The precursor solution-loaded carbon black was sonicated for 2 h, and then freeze-dried to obtain precursor-loaded carbon black powders prior to the high-temperature shock synthesis.[11] The dried powders were evenly spread on the carbon paper heater,[49] and then Joule-heated in Ar-filled glovebox by a high-temperature thermal shock (~2000 K, ~1 s).

Structural and morphological characterization

Elemental analysis was performed in a scanning electron microscope (SEM, JSM-5800LV, JEOL Japan) equipped with an energy dispersive X-ray spectrometer (EDX, INCA with Suite 4.13 analysis software, Oxford Instruments, UK). Data was acquired applying an accelerating voltage of 20 kV.

Surface composition of all samples was analyzed with X-ray photoelectron spectroscopy (XPS). The XPS measurements were performed by a PHI Quantera II scanning XPS microprobe (Physical Electronics, ULVAC-PHI). The carbon-supported powder samples and the sputtered samples were fixed on the sample holder with double-sided copper tape, where the powder samples were immobilized on top of the adhesive tape. The spectra were acquired using Al Kα irradiation, and a circular area of 200 μm diameter was irradiated at 50 W and 15 kV. The survey scans were acquired at 280 eV pass energy with a step size of 0.5 eV. The resulting data was analyzed by CasaXPS (V.2.3.18), using instrument-specific relative sensitivity factors, Shirley backgrounds, and a binding energy scale calibrated to the adventitious carbon peak at 284.8 eV.

Morphological aspects of the carbon-supported electrocatalyst samples were studied with transmission electron microscopy (TEM, JEOL 2100F FEG TEM operated at 200 kV). The particle size and distribution were achieved by using the Nano Measurer software.

High-angle annular darkfield (HAADF) scanning TEM (STEM) and spectrum imaging was performed using a Thermo Fisher Scientific Talos F200i (S)TEM operated at a primary electron energy of 200 keV. The microscope is equipped with a Dual Bruker XFlash 6 | 100 EDXS detector.

AFM measurements were performed on a WITec alpha 300RA atomic force microscope (WITec, Germany). The samples were scanned in contact mode, and the topography readout was used to determine the surface roughness. Five spots were analyzed per sample at a pixel size of 5 nm and within an image area of 0.25 × 0.25 μm^2. Raw data was processed using a line slope subtraction for accounting for sample stage tilt. The surface roughness was defined as the arithmetic mean of the absolute deviation from the mean sample height (R_a). R_a was calculated for each image per sample, and the final surface roughness is the arithmetic mean ± standard deviation of the five scans per sample.

Rotating disk electrode (RDE) measurements

General electrochemical behavior of both the sputtered thin-films and the carbon-supported nanoparticles was studied using a custom-designed Teflon RDE cell. Prior to measurements the cell was thoroughly cleaned. To remove organic contaminants, the cell was stored overnight in an acidified, saturated $KMnO_4$ solution. On the following day the cell was rinsed with dilute H_2O_2 solution, which was followed by a washing step with ultrapure water until the pH of the residual liquid was neutral. Finally, the cell was boiled in 1% HNO_3 for an hour, washed with ultrapure water four times and then boiled in ultrapure water for an additional hour. This final step ensured that all inorganic contaminants are dissolved. Between experiments the cell was boiled in 1% HNO_3 and in ultrapure water.

An RDE electrode was modified to be able to accommodate 5 × 5 mm silicon wafer pieces sputtered with the respective metal alloy sample. More details on the setup can be found elsewhere.[3] The resulting Kapton-coated geometric surface area of the electrode was 0.0314 cm^2.

In the case of the carbon-supported NPs, a glassy carbon (GC) RDE electrode (Pine Instruments) was directly used (A_{geo} = 0.1963 cm^2). The catalyst ink consisted of 5.65 mg of the given carbon-supported metal NPs, 0.8 mL H_2O, 0.2 mL isopropanol, and 10 μL Nafion. Inks were homogenized using a sonication horn (Branson SFX 150) for 40 min with 25% intensity. Sonication was turned on for 4s, which was followed by a break for 2 s 10 μL of the prepared ink was then drop-casted on the GC electrode and the ink was left to dry for at least 30 min in ambient conditions. All measured data was normalized against the geometric surface area. The prepared RDE tips were then immersed in the Teflon RDE cell filled with approx. 30 mL of either 0.1 M $HClO_4$ or with 0.05 M KOH electrolyte. A GC rod (SIGRADUR), and a Ag/AgCl/3M KCl (Metrohm) were used as the counter-, and reference electrodes. All reported potentials were converted to the reversible hydrogen electrode (RHE) scale. The RHE was measured daily on a commercial Pt RDE (Pine Instruments) to validate (and calibrate) the Ag/AgCl/3 M KCl reference electrodes. Electrochemical protocols were performed on a Biologic VSP-300 potentiostat. All RDE data presented in the manuscript are iR-corrected ($R_{s,sputtered\ films,\ acid} \approx 115\ \Omega$, $R_{s,sputtered\ films,\ alkaline} \approx 340\ \Omega$, $R_{s,\ NPs,\ acid} \approx 25\ \Omega$, $R_{s,\ NPs,\ alkaline} \approx 75\ \Omega$). The electrochemical protocol consisted of three cyclic voltammograms (CVs) recorded in between 0.05 V_{RHE} – 1.4 V_{RHE} applying 200 mV s^{-1} scan rate. The electrolyte in the cell was saturated with Ar 30 min prior to the measurements and Ar was kept purging in the headspace of the cell during performing the electrochemical protocols.

On-line ICP-MS measurements

The stability of the sputtered thin films and the carbon-supported metal NPs was investigated with on-line ICP-MS technique. The setup consists of a scanning flow cell (SFC), which outlet was coupled to the inlet of an inductively-coupled-plasma mass spectrometer (PerkinElmer NexION 350X) Identical electrolytes, counter-, and reference electrodes were used as for the RDE measurements. To avoid Cl^- contamination, the reference electrode was connected to the SFC on the outlet side through a capillary channel (providing close proximity to the surface of the working electrode) Further information on the setup can be found elsewhere.[45,77] The sputtered metal and metal-alloy thin films were used as the working electrode without any modification. A polished GC electrode (5 × 5 cm, SIGRADUR) served as the substrate in the case of the carbon-supported NPs. 0.2 μL aliquots from the previously prepared inks (ink recipe is similar to the one used during the RDE measurements) were drop-casted on the GC substrate and this was used as the working electrode. Each working electrode was placed on a 3D translational stage (Physik Instrumente M-403) allowing the fast navigation along the electrode and the rapid screening of multiple samples. All electrochemical measurements were performed using a Gamry ref. 600 potentiostat. All instruments (gas control box, mass flow controllers, peristaltic pump, stage) were controlled by a custom-made LabView software. The electrocatalyst stability was studied by performing two electrochemical protocols. The first protocol consisted of a potentiostatic hold at 0.05 V_{RHE} for 5 min, which was followed by a 10 min potentiostatic hold at 1.2 V_{RHE}. The protocol was finished with a potentiostatic hold at 0.05 V_{RHE} for 5 min. Similar to the first protocol, the second one was started with a 5 min potentiostatic hold at 0.05 V_{RHE}, which was followed by three CVs with gradually increasing potential limits (0.9, 1.2, and 1.5 V_{RHE}) applying 5 mV s^{-1} scan rate. The protocol was finished with a 3 min potentiostatic hold at 0.05 V_{RHE}.

ICP-MS was calibrated daily by a four-point calibration slope prepared from standard solutions that contained the metals of interest in a given concentration in either 0.1 M $HClO_4$-, or in 0.05 M KOH electrolyte. ^{187}Re (for ^{195}Pt and ^{193}Ir), ^{130}Te (for ^{108}Pd), ^{98}Mo (for ^{102}Ru), and ^{115}In (for ^{103}Rh) were used as internal standards. Internal standard solutions were prepared in 1% HNO_3 electrolyte and were introduced to the nebulizer of the ICP-MS via a Y-connector. The ICP-MS dwell time per AMU was set to 30 ms with 5 sweeps/reading. The Ar-purged electrolyte flow-rate was controlled by the peristaltic pump of the ICP-MS (Elemental Scientific M2) and calibrated daily. The average flow rate was 3.51 ± 0.1 μL s^{-1}. All measured data (both electrochemical and ICP-MS) were normalized with either the geometric surface area of the SFC (sputtered thin films, $A_{geo,SFC}$ = 0.0284 cm^2) or with the area of the drop-casted catalyst spot (carbon-supported NPs, measured individually by a laser scanning microscope – Keyence VK-X250).

QUANTIFICATION AND STATISTICAL ANALYSIS

All Figures and additional calculations were done by Origin from the raw data.

XPS data was analyzed by CasaXPS (V.2.3.18).

SEM-EDX data was analyzed using Suite 4.13 analysis software, Oxford Instruments, UK.

All presented error bars were calculated from at least two measurements, each one always performed on a fresh sample.